# From CloudSat-CALIPSO to EarthCare: Evolution of the DARDAR cloud classification and its comparison to airborne radar-lidar observations

Marie Ceccaldi, Julien Delanoë, R. J. Hogan, N. L. Pounder, Alain Protat, Jacques Pelon

JOURNAL OF GEOPHYSICAL RESEARCH: ATMOSPHERES, VOL. 118, 7962–7981, doi:10.1002/jgrd.50579, 2013

# From CloudSat-CALIPSO to EarthCare: Evolution of the DARDAR cloud classification and its comparison to airborne radar-lidar observations

M. Ceccaldi,[1] J. Delanoë,[1] R. J. Hogan,[2] N. L. Pounder,[2] A. Protat,[3] and J. Pelon[4]

Received 14 December 2012; revised 7 June 2013; accepted 20 June 2013; published 30 July 2013.

[1] This paper presents the implementation of a new version of the DARDAR (radar lidar) classification derived from CloudSat and CALIPSO data. The resulting target classification called DARDAR v2 is compared to the first version called DARDAR v1. Overall DARDAR v1 reports more cloud or rain pixels than DARDAR v2. In the low troposphere this is because v1 detects too many liquid cloud pixels, and in the higher troposphere this is because v2 is more restrictive in lidar detection than v1. Nevertheless, the spatial distribution of different types of hydrometeors show similar patterns in both classifications. The French airborne Radar-Lidar (RALI) platform carries a CloudSat/CALIPSO instrument configuration (lidar at a wavelength of 532 nm and a 95 GHz cloud radar) as well as an EarthCare instrument configuration (high spectral resolution lidar at 355 nm and a 95 GHz Doppler cloud radar). It therefore represents an ideal go-between for A-Train and EarthCare. The DARDAR v2 classification algorithm is adapted to RALI data for A-Train overpasses during dedicated airborne field experiments using the lidar at 532 nm and the radar Doppler measurements. The results from the RALI classification are compared with the DARDAR v2 classification to identify where the classification should still be interpreted with caution. Finally, the RALI classification algorithm with lidar at 532 nm is adapted to RALI with high spectral resolution lidar data at 355nm in preparation for EarthCare.

**Citation:** Ceccaldi, M., J. Delanoë, R. J. Hogan, N. L. Pounder, A. Protat, and J. Pelon (2013), From CloudSat-CALIPSO to EarthCare: Evolution of the DARDAR cloud classification and its comparison to airborne radar-lidar observations, *J. Geophys. Res. Atmos.*, *118*, 7962–7981, doi:10.1002/jgrd.50579.

## 1. Introduction

[2] Clouds play a major role in Earth's radiation budget, water cycle, and climate forecasts [*Stephens*, 2005; *Sun and Shine*, 1995]. Depending on their altitude and on their particle type, shape, size, and concentration, clouds have different impacts on absorption and reflection of short-wave incoming solar radiation and long-wave Earth-emitted radiation.

[3] Satellite data are vital in order to cover large areas globally (though they do not cover the poles) in a short period of time. CloudSat and CALIPSO (Cloud-Aerosol Lidar and Infrared Pathfinder Satellite Observations), part of the A-train constellation of satellites, were launched in April 2006 to study cloud and aerosol properties and the Earth radiation budget.

[4] CloudSat carries a 94 GHz CPR (Cloud Profiling Radar) [*Stephens et al.*, 2002]. CALIPSO boards CALIOP (Cloud-Aerosol Lidar with Orthogonal Polarization), a nadir-viewing two-wavelength (532 and 1064 nm), polarization-sensitive lidar and a three-channel IR (infrared) radiometer [*Winker et al.*, 2003, 2010]. Each of these instruments has their own strengths and weaknesses; combining them provides a more thorough picture of a cloud's structure and microphysical radiative properties. The synergy between radar, lidar, and infrared radiometers has proved effective for retrieving cloud properties [*Delanoë and Hogan*, 2008, 2010; *Deng et al.*, 2010; *Okamoto et al.*, 2010] provided that the location and the nature of hydrometeors are known. Indeed, particle size and IWC (ice water content)/LWC (liquid water content) retrieval methods use different microphysical assumptions depending on the assumed type of targets.

[5] Radar and lidar have complementary properties: In the Rayleigh scattering regime, when particles are much smaller than the observing wavelength, the radar return signal is

[1]Laboratoire Atmosphères, Milieux, Observations Spatiales, Guyancourt, France.
[2]Department of Meteorology, University of Reading, Reading, UK.
[3]Centre for Australian Weather and Climate Research, Australian Bureau of Meteorology and CSIRO, Melbourne, Victoria, Australia.
[4]Laboratoire Atmosphères, Milieux, Observations Spatiales, Université Pierre et Marie Curie, Paris, France.

Corresponding author: M. Ceccaldi, Laboratoire Atmosphères, Milieux, Observations Spatiales, 11 Boulevard d'Alembert, FR-78280 Guyancourt, France. (marie.ceccaldi@latmos.ipsl.fr)


2169-897X/13/10.1002/jgrd.50579

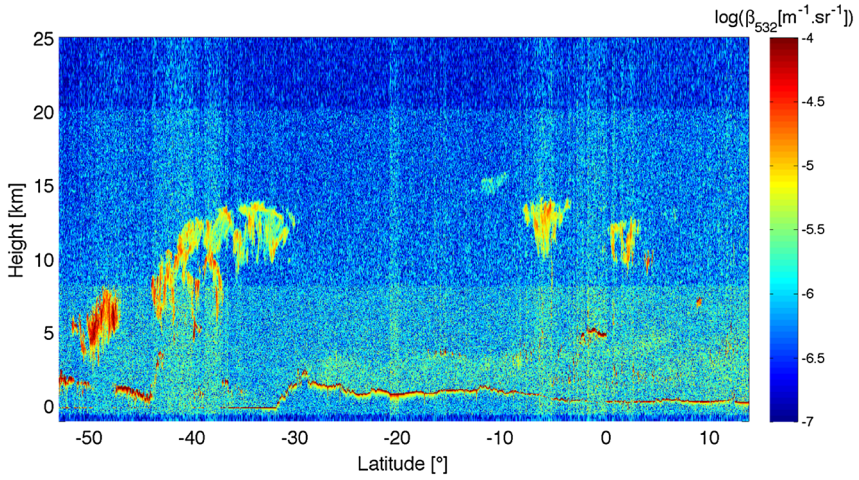


**Figure 1.** CALIPSO daytime signal at 532 nm for granule 05725 on 26 May 2007.

proportional to the sixth moment of the particle size distribution; hence, within a volume it is most sensitive to the largest particles. On the other hand, lidar backscatter is proportional to the second moment of the particle size distribution; therefore, it is most sensitive to particle concentration and backscattering cross section. Lidar signals are sensitive to optically thin clouds but are rapidly attenuated in optically thick clouds, whereas radar signals are able to penetrate even

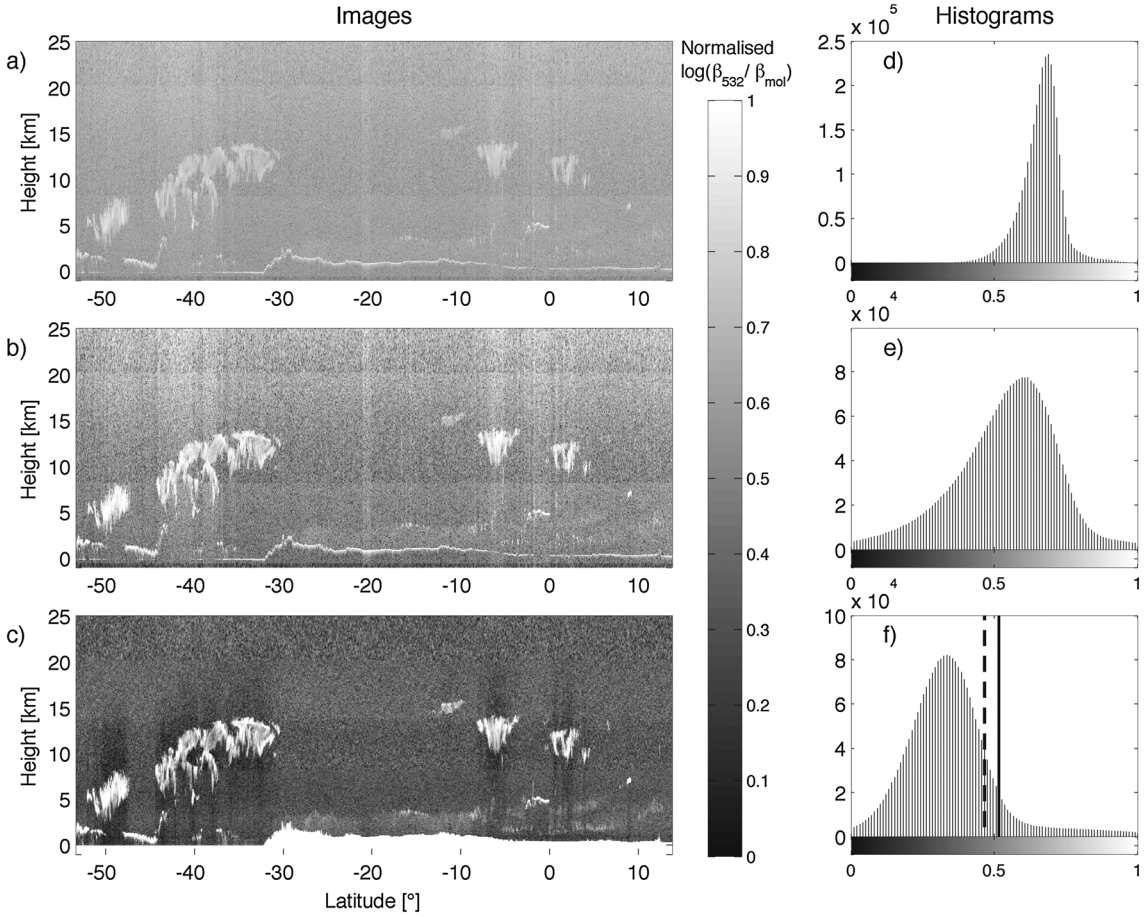


**Figure 2.** Processing flow for daytime lidar image of granule 05725. (a) Grayscale image of $\log(\beta_{532}/\beta_{\mathrm{mol}})$. (b) Enhanced image smoothed with a moving average filter. (c) Figure 2b filtered in the frequency domain. (d, e, and f) The 0 km to 8.2 km histograms of $\log(\beta_{532}/\beta_{\mathrm{mol}})$ values in Figures 2a–2c, respectively, with aerosol (dashed line) and cloud (solid line) thresholds in the histogram in Figure 2f.

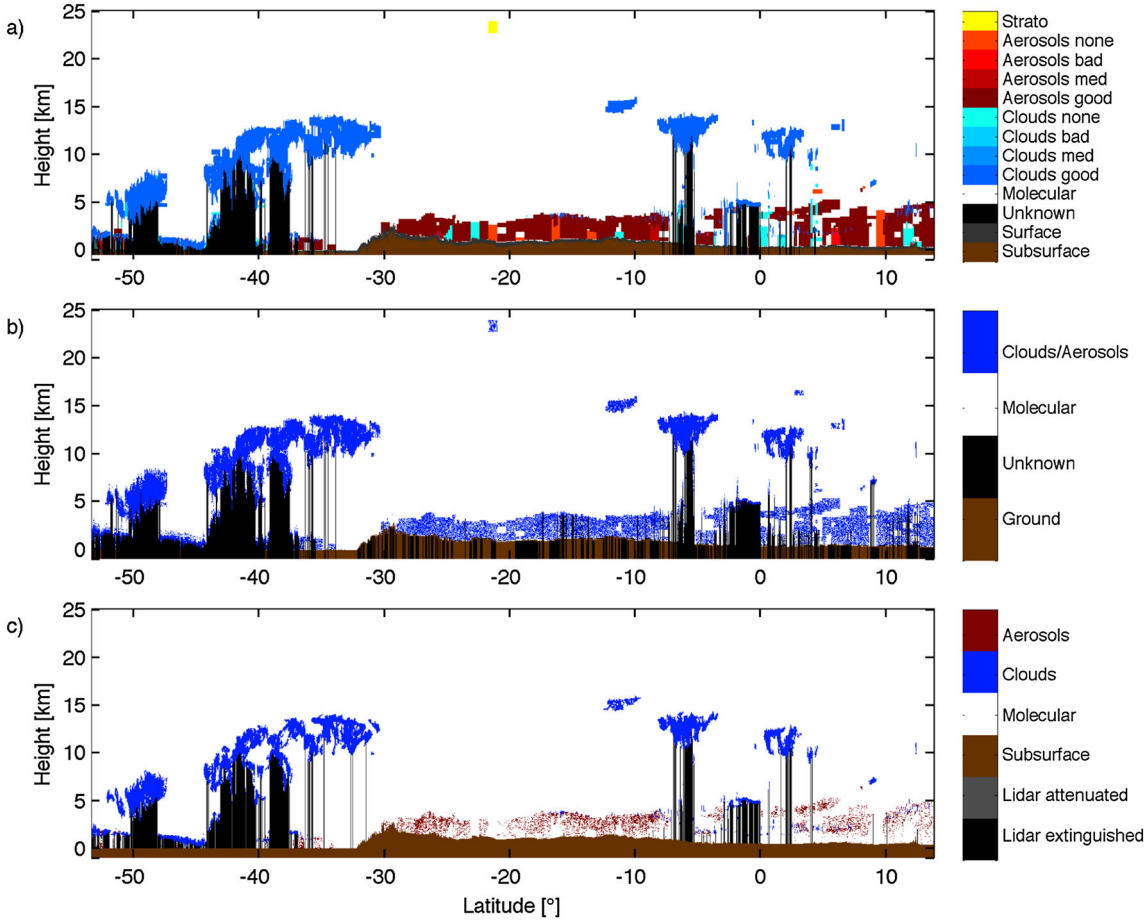


**Figure 3.** Comparison of lidar masks from (a) VFM categorization, (b) DARDAR v1 lidar mask, and (c) DARDAR v2 lidar mask.

optically thick clouds, such as liquid water clouds, but are less sensitive to optically thin clouds composed of small particles.

[6] DARDAR (radar lidar) is a project initiated by the LATMOS and the University of Reading to provide collocated CloudSat, CALIPSO, and MODIS (Moderate Resolution Imaging Spectroradiometer) measurements as well as a cloud classification and ice cloud retrievals on a 60 m vertical resolution and 1 km horizontal resolution grid [*Delanoë and Hogan*, 2010]. Before inferring cloud properties from radar and lidar profiles, it is necessary to develop a reliable method to locate and identify the type of targets detected. The first DARDAR CloudSat-CALIPSO target classification (hereafter called DARDAR v1) was originally developed because neither radar and lidar collocated data nor combined categorization on such a fine grid are available in the NASA official products. The NASA CloudSat Data Processing Center provides Level 2 products, such as 2B-GEOPROF, containing information on the nature of targets in the profiles, as well as CloudSat-CALIOP synergetic products data such as 2B-GEOPROF-LIDAR, but these are not available on the same resolution grid as DARDAR. Although DARDAR v1 is widely used [*Delanoë et al.*, 2011; *Stein et al.*, 2011a, 2011b; *Huang et al.*, 2012; *Delanoë et al.*, 2013; *Jouan et al.*, 2012], it has several points which require improvements. Moreover, the forthcoming ESA (European Space Agency)/JAXA (Japan Aerospace Exploration Agency) mission EarthCare (Earth Clouds, Aerosols and Radiation Explorer), scheduled for the end of 2016, which goal is to study the role of clouds and aerosols in Earth's radiation budget, will board different instruments: ATLID, an atmospheric lidar with high spectral resolution (HSR) capabilities and depolarization channel at 355 nm; a cloud profiling radar (CPR) with Doppler measurements; a scanning multispectral imager (MSI); and a broadband radiometer (BBR) for top of the atmosphere radiation and fluxes (http://www.esa.int/esaLP/ASESMYNW9SC_LPearthcare_0.html). Therefore, having a classification method ready to be adapted to EarthCare data as soon as they are available would be beneficial. This is why the improved version of the DARDAR cloud classification, hereafter called DARDAR v2, was implemented.

[7] This paper describes how the DARDAR classification algorithm was modified in preparation for EarthCare and how it differs from the original version. This paper focuses only on the information that can be inferred from the lidar and radar data interpolated on a 60 m by 1 km resolution grid. Sections 2 and 3 present the DARDAR v2 classification method, and section 4 characterizes the differences between the two versions. In section 5 the DARDAR v2 algorithm is adapted and compared with the French airborne RALI

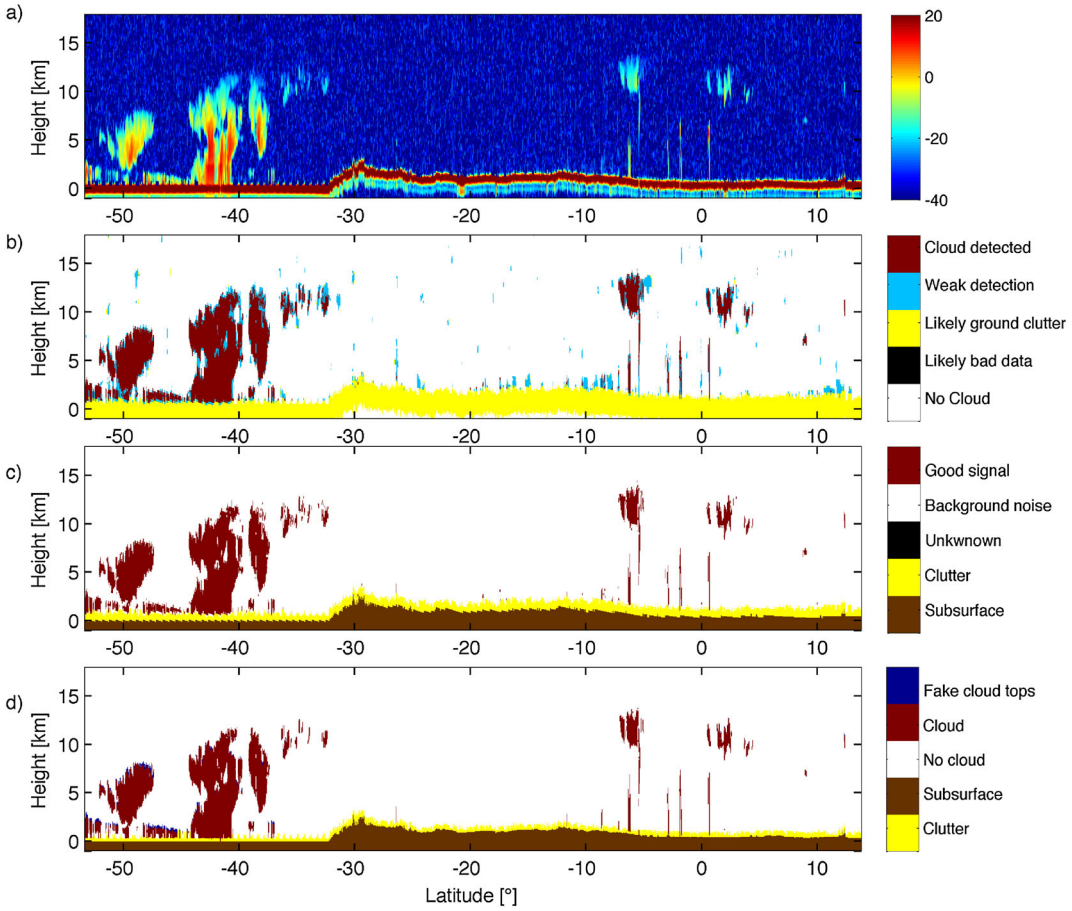


**Figure 4.** Comparison of radar masks with (a) CloudSat reflectivity [dBZ], (b) CloudSat radar mask with weak detection corresponding to mask values between 6 and 10 and cloud detection with mask values above 30, (c) DARDAR v1 radar mask, and (d) DARDAR v2 radar mask.

instruments [*Protat et al.*, 2004; *Delanoë et al.*, 2013], which are also used to prepare for the EarthCARE mission.

## 2. Data Set and Masks Implementation

### 2.1. CloudSat and CALIPSO Data Sets

[8] We use the data set described in [*Delanoë and Hogan*, 2010], available from the ICARE (Interactions Clouds Aerosols Radiations Etc) Thematic Centre (http://www.icare.univ-lille1.fr/). The ICARE Thematic Centre provides Multi Sensor "CS-TRACK-UNIT" data. These data, originally provided by the CloudSat data center and the NASA Langley Centre, are preprocessed so that A-train measurements, NASA official Level 2 products, and ancillary data are collocated within the CloudSat footprints (1.1 km) with profiles at a 60 m vertical resolution. This is the DARDAR resolution grid. The altitude range of the data is –1.02 km to 25.08 km, and the latitude range is –82° to 82° (see *Delanoë and Hogan* [2010] for further details).

[9] To develop the new DARDAR classification version, we use input from a number of "CS-TRACK-UNIT" data products, all available from the ICARE ftp website. The lidar attenuated backscatter coefficient, $\beta$, at 532 nm comes from the CALIPSO Level 1B profile data and the 94 GHz radar reflectivity, Ze, from the CloudSat 2B GEOPROF product. These data are already calibrated [*Winker et al.*, 2007; *Tanelli et al.*, 2008; *Protat et al.*, 2009]. Thermodynamic variables like temperature, pressure, and specific humidity come from the ECMWF (European Center for Medium-Range Weather Forecasts)-AUX unit file. The CALIPSO VFM (Vertical Feature Mask), available in the file CS-TRACK-UNIT-CAL-LID-L2-VFM, gives information on the nature of targets in the lidar profiles with a quality flag. Even if it is interpolated on the "CS-TRACK-UNIT" resolution grid, it still presents very large block effect due to the spatial and vertical averaging used to increase the signal-to-noise ratio. Therefore, on the DARDAR resolution grid, some noise pixels are inevitably included in the VFM clouds, and these cannot be used in the inverse method used for ice clouds retrievals, but it is still useful for us to distinguish clouds from aerosols.

### 2.2. Lidar Mask

[10] Our work is primarily focused on clouds so we have not developed an independent method to discriminate clouds from aerosols in lidar data but rather use the VFM. In DARDAR v2, only aerosols that are detectable at the DARDAR resolution are included, resulting in far less aerosol than in averaged products such as the VFM. Users interested in aerosols should use the official CALIOP product.

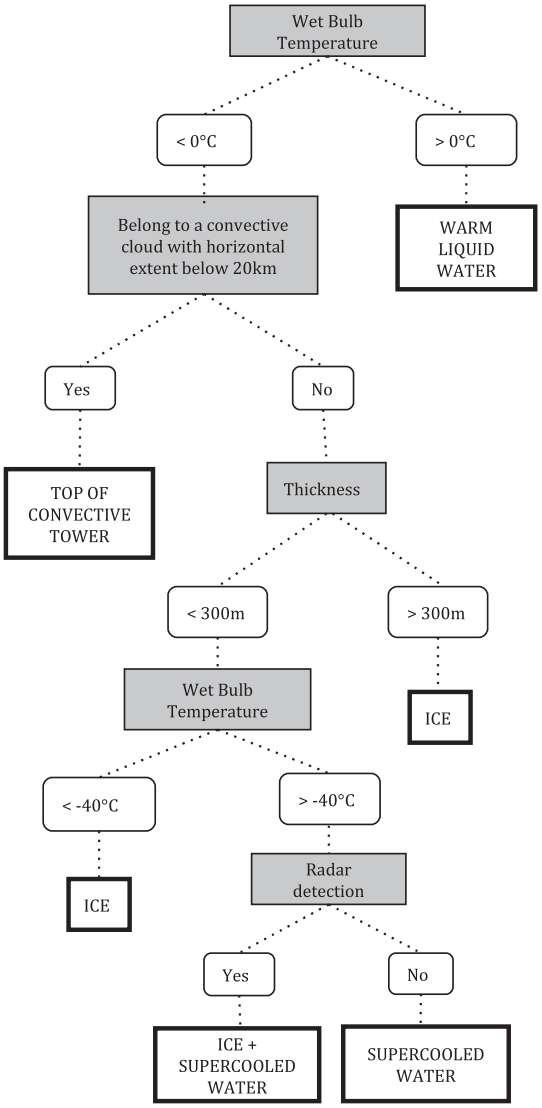


**Figure 5.** Decision tree for classifying layers with a strong backscatter signal.

[11] We use only the 532 nm CALIOP channel because this wavelength is more sensitive to small particles, and hence aerosols and optically thin clouds composed of small particles, than the 1064 nm channel. Figure 1 shows the return signal at 532 nm, hereafter $\beta_{532}$, from granule 05725 on 26 May 2007. The daytime lidar signals are particularly noisy due to solar radiation. Darker and brighter stripes appear according to changes in scene reflectance. The lidar calibration is assumed to be correct, but we note that miscalibration could lead to biases in the feature masks.

[12] The technique to select the pixels containing clouds or aerosols relies on thresholding grayscaled images of $\log(\beta_{532}/\beta_{mol})$ with $\beta_{532} > 0$. $\beta_{mol}$ is the modeled molecular backscattering at 532 nm calculated from temperature and pressure and is used to remove the molecules' contribution in the lidar signal. This technique is applied granule after granule.

[13] Each granule is first split into three parts (first night segment, day segment, and last night segment), each treated independently. Before thresholding, image processing is applied to the original three day and night images in a series of steps, as shown in Figure 2 for a daytime example. Once processed, these three images are vertically split into three parts (0 km to 8.2 km, 8.2 km to 20.2 km, and 20.2 km to 25 km) according to the original vertical averaging of CALIOP data for thresholding.

[14] In Figure 2a, showing the original normalized image (with values between 0 and 1), the contrast between noise and clouds is poor, and this is confirmed by the narrowness of the image histogram in Figure 2d. The histograms in Figures 2d, 2e, and 2f are the histograms of the $\log(\beta_{532}/\beta_{mol})$ values in the 0 km to 8.2 km image parts; in this specific example, they are well representative of the histogram of the full day image. The poor contrast makes it difficult to find an adequate threshold to extract clouds. To improve the contrast, the histogram is stretched and a moving average filter with a 9 pixel window is applied to reduced speckle. The results of this processing are displayed in Figures 2b and 2e. The contrast is increased, and the histogram now spreads over the full range from 0 to 1, but intensities of vertical noise stripes are consequently exaggerated. As this problem is not present at night, the nighttime image processing is stopped at this point. Finally, the daytime images are transformed to their frequency domain with a bidimensional discrete Fourier transform (DFT). On these frequency domain images, each pixel represents a frequency contained in the original spatial image. Before applying the inverse transformation to go back to spatial domain, we masked out the center horizontal and vertical lines of the frequency domain image. This removes all horizontal and vertical periodicity in the new spatial image, therefore reducing vertical and horizontal noise variations and minimizing the vertical striping. Figures 2c and 2f show the final image and corresponding histogram, in which the cloudy pixel values are more easily identifiable.

[15] The threshold is subsequently applied to each of the nine images composing the full granule. The first step is to select the detectable aerosol pixels. The histogram in Figure 2f is dominated by a strong mode centered at 0.42 corresponding to noise pixels. The aerosol threshold detection was chosen empirically as the intensity for which the number of pixels is equal to half the maximum height of

**Table 1.** Aerosol/Liquid Mask and Ice/Rain Mask Combination[a]

| | No Aerosol or Liquid | Liquid | Aerosols | Stratospheric | Extinguished |
|---|---|---|---|---|---|
| Ground | Ground (–1) | X | X | X | X |
| No ice or rain | Clear sky (0) | Liquid clouds (11) | Aerosols (6) | X | Do not know (–2) |
| Ice | Ice clouds (1) | Liquid cloud + ice (4) | X | Stratospheric (8) | Ice clouds (1) |
| Warm rain | Warm rain (7) | Liquid cloud + warm rain (12) | X | X | Warm rain (+liquid) (14) |
| Cold rain | Cold rain (5) | Liquid cloud + cold rain (13) | X | X | Cold rain (5) |

[a]Numbers in parentheses correspond to the number of the class.

**Table 2.** DARDAR v2 Classes

| Class Number | Definition |
|---|---|
| –4 | Clutter |
| –3 | Lidar extinguished |
| –2 | Lidar attenuated |
| –1 | Surface and subsurface |
| 0 | Clear sky |
| 1 | Ice |
| 2 | Lidar ice with depolarization ratio < 0.2 |
| 3 | Supercooled water |
| 4 | Supercooled water + ice |
| 5 | Cold rain from ice clouds |
| 6 | Aerosols |
| 7 | Warm rain/drizzle |
| 8 | Stratospheric features |
| 9 | High ice concentration layers |
| 10 | Strong backscatter convective towers top |
| 11 | Liquid water clouds |
| 12 | Warm rain + liquid cloud |
| 13 | Cold rain + liquid cloud |
| 14 | Warm rain (could be mixed with liquid) |

**Table 3.** DARDAR v1 Classes

| Class Number | Definition |
|---|---|
| –2 | Do not know |
| –1 | Surface and subsurface |
| 0 | Clear sky |
| 1 | Ice clouds |
| 2 | Supercooled water + ice |
| 3 | Liquid water |
| 4 | Supercooled water |
| 5 | Rain or drizzle |
| 6 | Aerosols |
| 7 | Possibly insects |
| 8 | Stratospheric features |

the histogram (on the right side of the mode). This limit is shown by the dashed vertical line in Figure 2f. The pixels with an intensity greater than this limit are considered to be likely clouds or aerosols. This is where we use the VFM to distinguish clouds from aerosols: any of these pixels classified as aerosol in the CS-TRACK-VFM (with either a bad, medium, or good quality flag), is then classified as aerosol in the DARDAR v2 classification. The detection is therefore done at the DARDAR resolution grid, but the attribution to aerosols is done with the VFM.

[16] In the same way, we chose the threshold for cloud detection empirically after testing several options: we selected the threshold for which the detected pixels corresponded to the clouds identified visually on the images. This threshold is represented by the solid vertical line in Figure 2f. It was chosen as the intensity for which the number of pixels is equal to a fifth of the maximum of the histogram. Any pixel whose intensity is greater than this threshold is classified as clouds. At this point, the lidar mask still contains noise pixels, so a final test on backscatter is performed to remove any falsely detected pixels. The logarithm of the backscattering value of each selected pixel, $\beta_{pix}$, is compared to the mean of the logarithm of the backscattering value of its 24 surrounding cloud or noise pixels, $\beta_{cloud}$ and $\beta_{noise}$, respectively. If $\beta_{pix} \leq \beta_{cloud} - 1.5$ or if $|\beta_{cloud} - \beta_{noise}| \leq 0.3$ (1.5 and 0.3 values are chosen empirically), then the center pixel is removed from the cloud mask. Also, every isolated cloud pixel is removed from the mask. This thresholding technique was tested on several case studies and found consistent with what is observed by eye.

[17] The lidar mask also contains areas of indetermination. When the lidar signal is too attenuated to detect the surface then all pixels below the last detected pixel are classified as "Lidar extinguished." When the lidar still detects the surface but misses some features detected by the radar, then pixels are classified as "lidar attenuated," but it is impossible to quantify to what extent the lidar is attenuated.

[18] The ground is located from the DEM (Digital Elevation Model) of the L1 Lidar file.

[19] Figure 3a shows the VFM and Figures 3b and 3c respectively the DARDAR v1 and v2 lidar mask. v1 includes more pixels than v2. This is because v1 relies on the VFM that has a block effect (that is, clouds and aerosols presenting square features) effect due to the VFM spatial averaging increasing the number of cloud or aerosol pixels, whereas v2 only relies on 60 m vertical resolution lidar profiles. Note the presence of a square stratospheric cloud in the VFM and v1 around –20° where there is no obvious trace of it in Figure 1. The statistical differences between the two versions will be fully investigated in section 4.1, but we can already say that on this specific example we count 3.69% of cloud or aerosols pixels in DARDAR v2, 4.86% in DARDAR v1, and 5.33% in the VFM.

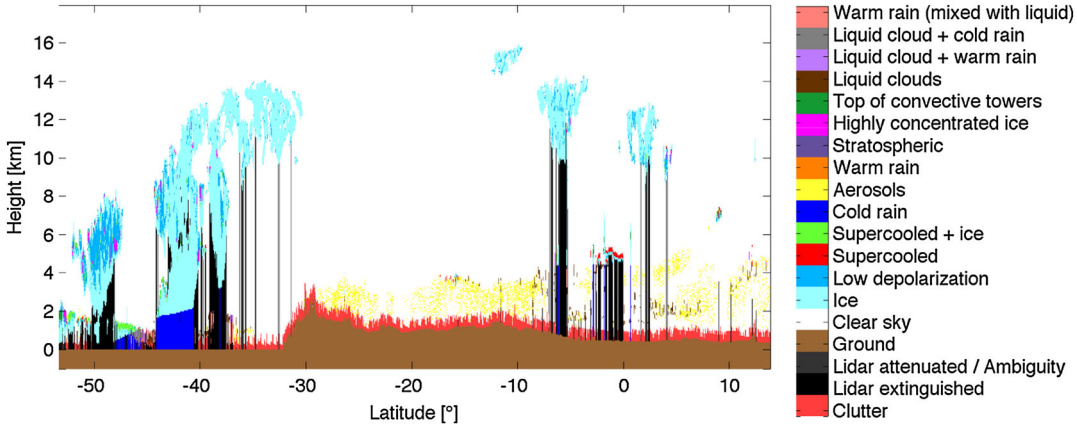


**Figure 6.** DARDAR v2 classification sample of granule 05725 on 26 May 2007.

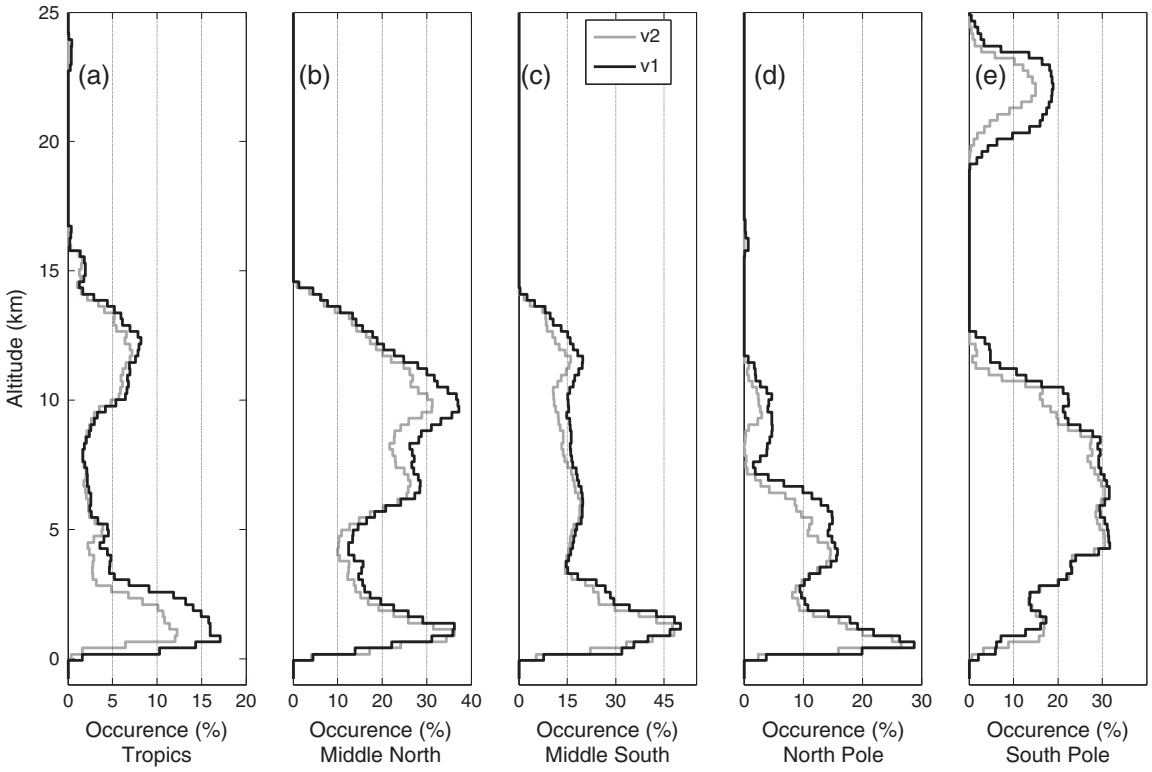


**Figure 7.** Histogram with respect to altitude of cloud or rain occurrence for the two DARDAR classifications for the granule 05725 on 26 May 2007 in (a) the tropics, (b) the middle northern latitudes, (c) the middle southern latitudes, (d) the North Pole, and (e) the South Pole.

### 2.3. Radar Mask

[20] Cloud detection from radar reflectivity relies on thresholding in the same way as for the lidar mask. We found that for radar the adequate threshold for cloud detection is the intensity for which the number of pixels is equal to a sixth of the maximum of the histogram. In the resulting mask, we remove the false radar detection caused by the 500 m original vertical resolution brought on to a 60 m vertical resolution with the help of the lidar mask. When the lidar is not extinguished, it always detects the tops of clouds seen by the radar. Therefore, all radar detection above the lidar cloud top are removed from the mask. This correction is important because a fake radar cloud top would introduce a bias in climatologies.

[21] Any pixel less than 1.2 km aboveground with reflectivity higher than 15 dBZ is considered radar clutter. Also, in the same area, any pixel with reflectivity higher than the detection threshold is considered radar clutter unless every pixel below 1.2 km in the vertical column is above the detection threshold. In this case, we consider that they belong to cloud or rain.

[22] CloudSat data center provides a mask giving information of location of likely hydrometeors [*Marchand et al.*, 2008]. The mask values, ranging from 0 to 40, give an indication of the confidence with which we can report a radar detection. Figure 4a shows the CloudSat reflectivity in dBZ, Figure 4b is the corresponding radar mask from the CloudSat data center, and Figures 4c and 4d are, respectively, the radar masks from DARDAR v1 and v2. In Figure 4b, "Weak detection" includes the CloudSat mask values ranging from 6 to 10 and "Cloud detected" the values above 30, which is the most widely used threshold for confident cloud detection. In the v1 radar mask, ground and clutter are refined from the CloudSat mask. When the cloud features in the v1 radar mask have a common boundary with the clutter, then all pixels below the boundary until the ground are considered as good targets to be classified in the DARDAR v1 classification.

[23] The radar mask from DARDAR v1, DARDAR v2, and CloudSat are very similar. The percentage of pixels in the daytime granule that are either cloud or rain in each of the DARDAR v1, DARDAR v2, and CloudSat mask are 4.59%, 4.61%, and 5.03%, respectively. This slight difference is due to the corrected cloud tops and because the CloudSat mask is slightly less restrictive than DARDAR.

## 3. Target Categorization

### 3.1. Strong Lidar Backscatter Layers

[24] Lidar backscatter intensity contains information about the nature of the hydrometeors. Strong backscatter regions are composed either of warm liquid water, supercooled water, ice in high concentration, or a mix of them. Locating supercooled water layers is crucial as they represent a major weather hazard in aeronautics and can cause fatalities [*Reehorst et al.*, 2008]. Moreover, they have an

influence on retrieval methods [*Delanoë and Hogan*, 2010] and radiative transfer calculations [*Hogan et al.*, 2003]. Such hydrometeors have the power to extinguish the lidar signal or at least to strongly attenuate it. *Delanoë and Hogan* [2010] and *Zhang et al.* [2010] both describe a method to identify supercooled water layers. These layers are usually physically thin (no more than 300 m) and observed in regions where the temperature is lower than 0°C and higher than –40°C [*Hogan et al.*, 2004; *Zhang et al.*, 2010], which is the homogenous nucleation temperature.

[25] In DARDAR v2, we locate any type of attenuating high backscatter layer ($\beta_{532} > 2.10^{-5}$ m$^{-1}$ sr$^{-1}$ [*Delanoë and Hogan*, 2010]) and then classify them according to temperature and parameters from the radar and lidar masks.

[26] These layers include any pixel where $\beta_{532} > 2.10^{-5}$ m$^{-1}$ sr$^{-1}$ and where $\beta_{532}$ drops by a factor of 10 in the next 480 m. The vertical extent of the layers is defined with the gates of maximum gradient in $\beta_{532}$ in the 240 m below and 300 m above each of these pixels.

[27] Before November 2007 the CALIOP pointing angle was almost at nadir but was tilted 3° off nadir after that. Horizontal ice crystal plates induce strong returns when viewed in the nadir configuration but not when viewed off nadir [*Zhou et al.*, 2012]. The technique used in *Delanoë and Hogan* [2010] to identify supercooled water was tested before and after the tilt, and no large difference was observed.

[28] Each of these strong backscatter layers is then treated separately to classify its pixels into five groups: (1) warm liquid water, (2) supercooled water, (3) supercooled water mixed with ice, (4) highly concentrated ice, and (5) top of updrafts in convective towers.

[29] The decision tree presented in Figure 5 classifies these layers based on the following criteria: temperature, horizontal extent of layer, thickness, reflectivity, and, for convective towers, location. If the ECMWF wet bulb temperature (temperature of adiabatic saturation) is greater than 0°C, then the layer is composed of warm liquid water. The upper part of strong updrafts in convective towers can be composed of liquid droplets and ice in different proportion, so these layers are categorized in a separate class. If the layer is less than 20 km wide and located in a vertically oriented cloud whose reflectivity is greater than 5 dBZ, then it is classified as top of updraft in convective tower (hereafter called top of convective tower). Doppler radar gives information on particle terminal fall velocity, and, therefore, precipitation and updraft areas will be more easily identified when EarthCare Doppler radar data are available. The remaining layers are classified as ice in high concentration if the layer is more than 300 m thick and/or if the wet bulb temperature is lower than –40°C and as supercooled water otherwise. The radar is not able to detect pure supercooled water because its signal is dominated by larger and less numerous particles [*Hogan et al.*, 2003]. So, if the radar detects a signal collocated with supercooled water layers detected by the lidar, they are classified as supercooled water mixed with ice.

[30] DARDAR v1 only selects the layers of supercooled water (mixed with ice or not). These layers often include a pixel above the actual increase in backscatter and below the actual drop off in backscatter. This tends to increase the supercooled water occurrence and fraction: over 3 months

**Table 4.** v1 and v2 Classifications Simplified Contingency Table for Granule 05725 on the 26.05.07[a]

| – | Unknown | Surface | Clear Sky | Ice | Supercooled+ice | Liquid | Supercooled | Rain | Aerosols | Strato | Total | Agree |
|---|---|---|---|---|---|---|---|---|---|---|---|---|
| Unknown | **236,218** | 21,247 | 66,652 | 19,510 | 3 | 673 | 16 | 13,286 | 902 | 0 | 358,507 | 65.89% |
| Surface | 5,896 | **935,360** | 48 | 1,207 | 11 | 221 | 1,185 | 1,469 | 0 | 0 | 945,397 | 98.94% |
| Clear sky | 83,987 | 85,517 | **13,162,126** | 21,649 | 22 | 4,285 | 260 | 389 | 12,988 | 482 | 13,371,705 | 98.43% |
| Ice | 14,701 | 2,851 | 142,439 | **762,813** | 5,989 | 0 | 1,364 | 0 | 417 | 0 | 930,574 | 81.97% |
| Supercooled+Ice | 2 | 186 | 4,296 | 16,738 | **15,371** | 4 | 1,717 | 0 | 41 | 0 | 38,355 | 40.08% |
| Liquid | 10,003 | 10,752 | 27,651 | 1,020 | 4 | **26,308** | 959 | 1,578 | 1,570 | 0 | 79,845 | 32.95% |
| Supercooled | 42 | 1,922 | 5,771 | 7,563 | 1,555 | 3 | **17,762** | 0 | 16 | 0 | 34,634 | 51.28% |
| Rain | 11,084 | 2,405 | 3,837 | 1 | 0 | 1,573 | 0 | **96,268** | 161 | 0 | 115,329 | 83.47% |
| Aerosols | 1,760 | 45,079 | 105,091 | 106 | 0 | 1,203 | 114 | 394 | **70,014** | 0 | 223,761 | 31.29% |
| Insects | 154 | 59 | 2,908 | 2 | 0 | 1,162 | 0 | 0 | 84 | 0 | 4,369 | 0% |
| Strato | 0 | 0 | 30,652 | 0 | 0 | 0 | 0 | 0 | 0 | **34,188** | 64,840 | 52.73% |
| Total | 363,847 | 1,105,378 | 13,551,471 | 830,609 | 22,955 | 35,432 | 23,377 | 113,384 | 86,193 | 34,670 | | |
| Agree | 64.92% | 84.62% | 97.13% | 91.84% | 66.96% | 74.25% | 75.98% | 84.90% | 81.23% | 98.61% | | |

[a]The lines correspond to the v1 classes and the columns to the v2 classes.The bold values correspond to the number of pixels classified in the same class in both DARDAR versions. For instance in the box of "Ice" line and "Clear Sky" column, we find the number 142,439, meaning that there are 142,439 pixels which were classified as ice in v1 which are now classified as clear sky in v2.

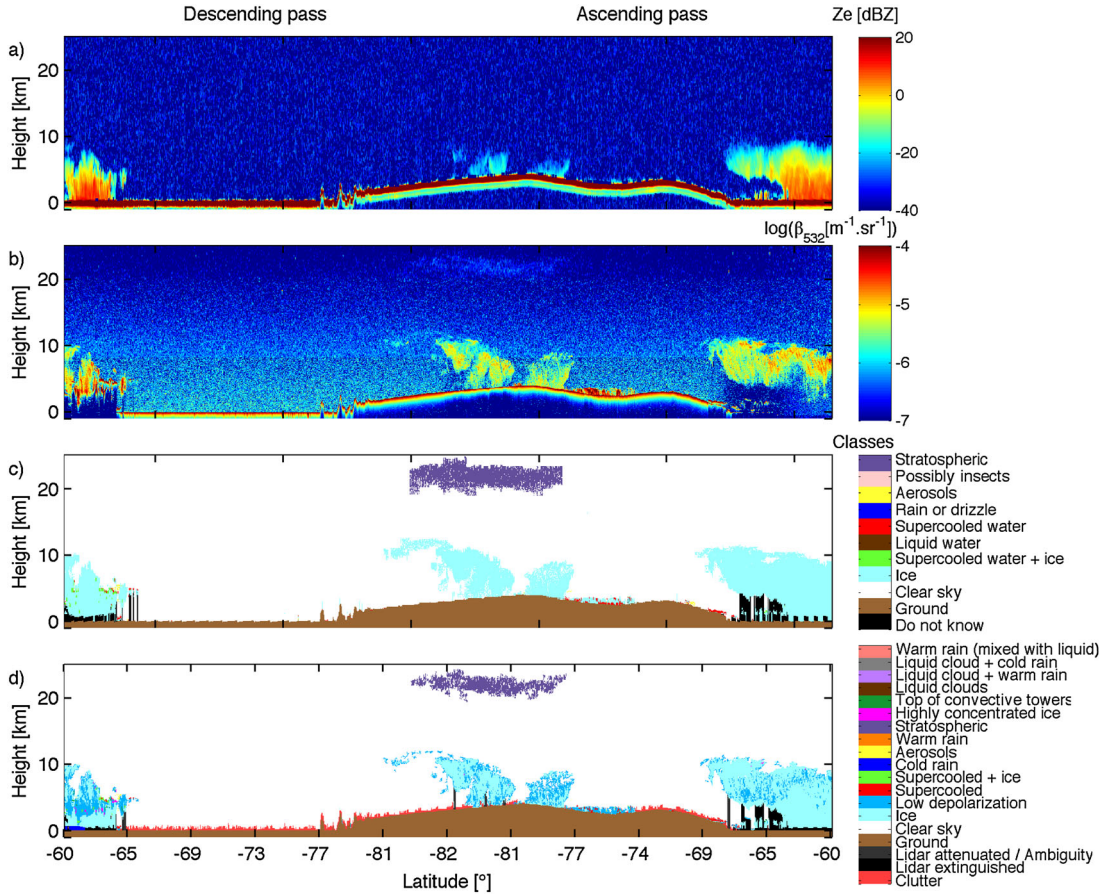


**Figure 8.** Comparison of (a) the CPR reflectivity Ze [dBZ], (b) the logarithm of the CALIOP attenuated backscatter coefficient $\beta_{532}$[m$^{-1}$ sr$^{-1}$], (c) DARDAR v1 classification, and (d) DARDAR v2 classification at the South Pole.

of data, v1 reports 1.8 times more supercooled water (mixed with ice or not) than v2, and we expect v2 to be more realistic.

### 3.2. Creation of DARDAR v2 Categorization

[31] Categorization is based on Table 1, which is a simplified version of the table presented in the target classification product for EarthCare described in *Delanoë et al.* [2010]. We created an aerosol/liquid mask and an ice/rain mask, from which many combinations, even mixed phase, are possible. Note that snow is not included in the DARDAR categorization because in microphysical properties retrieval methods we consider that there is a continuum between ice cloud and snow.

[32] In a warm atmosphere (ECMWF wet bulb temperature greater than 0°C), we distinguish precipitating from nonprecipitating clouds using the CloudSat reflectivity. Using CloudSat data, *Stephens and Haynes* [2007] report that for reflectivities below –15 dBZ the amount of drizzle is negligible, but *Leon et al.* [2008] sets this limit to –18 dBZ in marine stratocumulus clouds. In some other studies this limit varies between –15 dBZ and –20 dBZ [*Liu et al.*, 2008] for different types of radar at different wavelengths. We have chosen a threshold of Ze = –17 dBZ because it lies between all of these values.

[33] Cold rain is defined by a radar signal detection with Ze $\geq$ –17 dBZ located in a warm atmosphere and originating from ice clouds, whereas warm rain (or drizzle) is a radar signal detection with Ze $\geq$ –17 dBZ not coming from ice. If a cold rain pixel is observed, then all pixels below it until the ground are classified as rain even when marked as clutter or in cases where Ze decreases when reaching ground. This phenomenon can appear (more likely in the tropical regions) when rainwater evaporates before reaching the surface or when radar signal is attenuated by heavy convection and rain; the ground is then barely observable in the radar signal. We assume that the rain is falling vertically within the 1 km long gates. Radar mask pixels in a warm atmosphere, with Ze $\leq$ –17 dBZ, are assigned as liquid clouds. DARDAR v1 used the same ECMWF temperature data and the same reflectivity threshold to separate liquid clouds from precipitation but did not distinguish cold rain from warm rain.

[34] From Table 1, we have "cold rain and liquid cloud" when there is a good lidar signal and the radar reflectivity is above –17 dBZ. Note that we are not trying to give an estimate of cloud base as the lidar may be extinguished before actually reaching it. When the lidar is extinguished, the pixels are attributed to "cold rain" but they may be mixed with liquid in some areas close to the melting layer. Warm rain

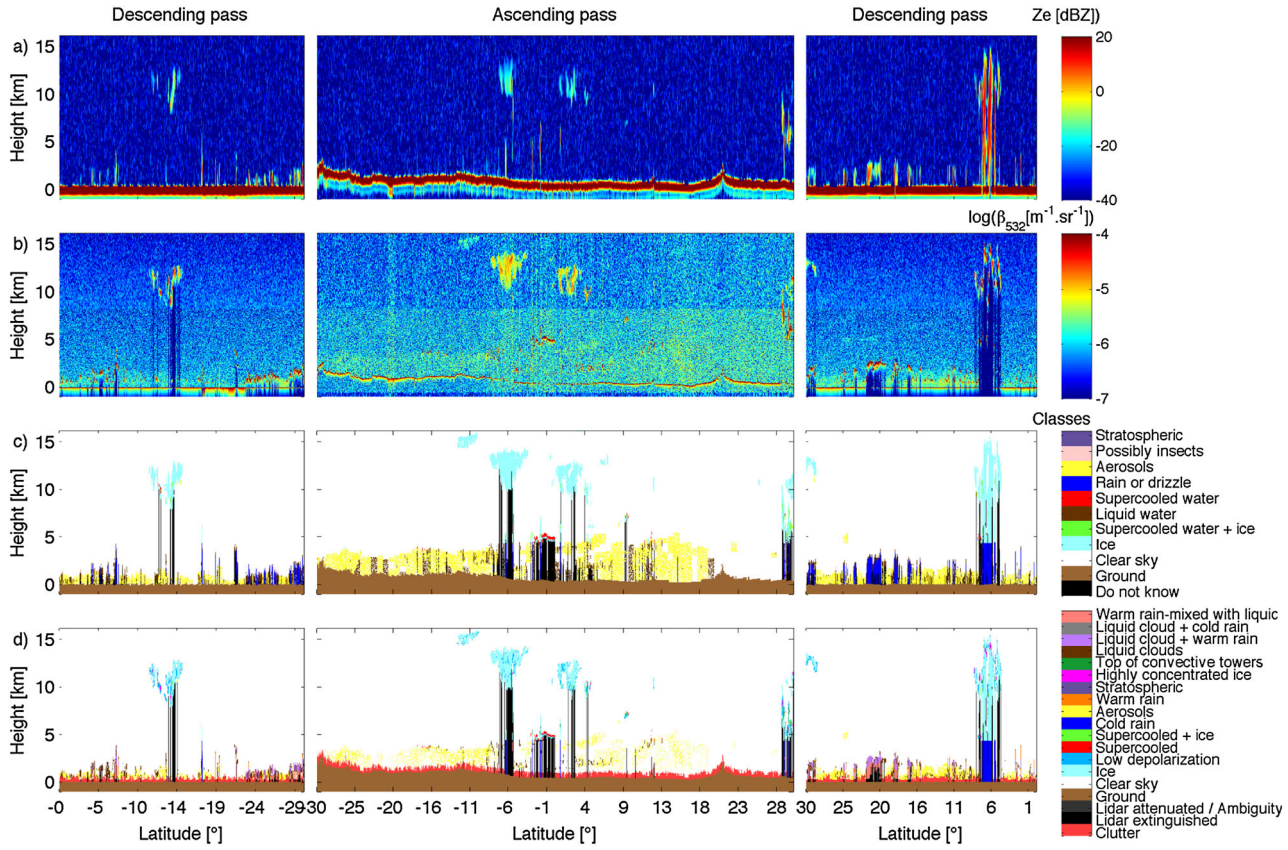


**Figure 9.** Comparison of (a) the CPR reflectivity Ze [dBZ], (b) the logarithm of the CALIOP attenuated backscatter coefficient $\beta_{532}$[$m^{-1}$ $sr^{-1}$], (c) DARDAR v1 classification, and (d) DARDAR v2 classification in the tropics.

pixels found in extinguished or attenuated lidar zones are categorized as "rain which could be mixed with liquid."

[35] Any feature detected by the lidar in the ice class and in the ice/rain mask situated above the lower limit of the stratosphere is classified as "stratospheric feature." We define the stratosphere lower limit as 3 km above the tropopause. The altitude of the tropopause is usually available in the CALIPSO L1 product, but when it is not, we define it as the height of minimal temperature on the vertical profile. It can happen that the temperature profile presents no minimum; in that case, the whole profile is described as troposphere.

[36] We also create a class for ice with low depolarization ratio. A low total depolarization ratio (we use a depolarization ratio < 0.2 for this class) can indicate that the ice particles' cross section is disk-shaped, meaning that the particles are either spherical or 2-D plates horizontally oriented [*Yoshida et al.*, 2010]. This class is only given as an indication since multiple scattering and daytime noise can influence the local inferred depolarization.

[37] DARDAR v2 classes are summarized in Table 2, and an example of the classification for a case study is shown in Figure 6. In this example many classes are represented: an area around –47° latitude shows liquid clouds in dark brown, liquid mixed with warm rain in purple and with cold rain in gray, as well as supercooled water mixed with ice in light green. Close to 0° latitude at 6 km there is a supercooled water layer in red. The radar clutter in dark orange is also well represented in this example.

## 4. Comparison Between DARDAR v1 and v2 Classifications

[38] This section focuses on the differences between the two DARDAR categorization versions. We first consider a case study of granule 05725 from 26 May 2007. We then look at the statistical distribution of hydrometeors from all the available data from January, February, and March 2010. Our aim is to analyze the differences and similarities between the two products; we do not produce a climatology nor do we study the spatial distribution of different cloud types.

### 4.1. Comparison of Classifications Using the Granule 05725 Case Study

[39] As reported in the previous sections, the technique used to categorize the targets in lidar and radar profiles are different in the two DARDAR versions. DARDAR v2 now introduces new classes, including mixed phase classes, making the v2 classification more precise. The DARDAR v1 classes are listed in Table 3.

[40] Figure 7 shows the occurrence of cloud or rain in granule 05725 as a function of altitude in different latitude

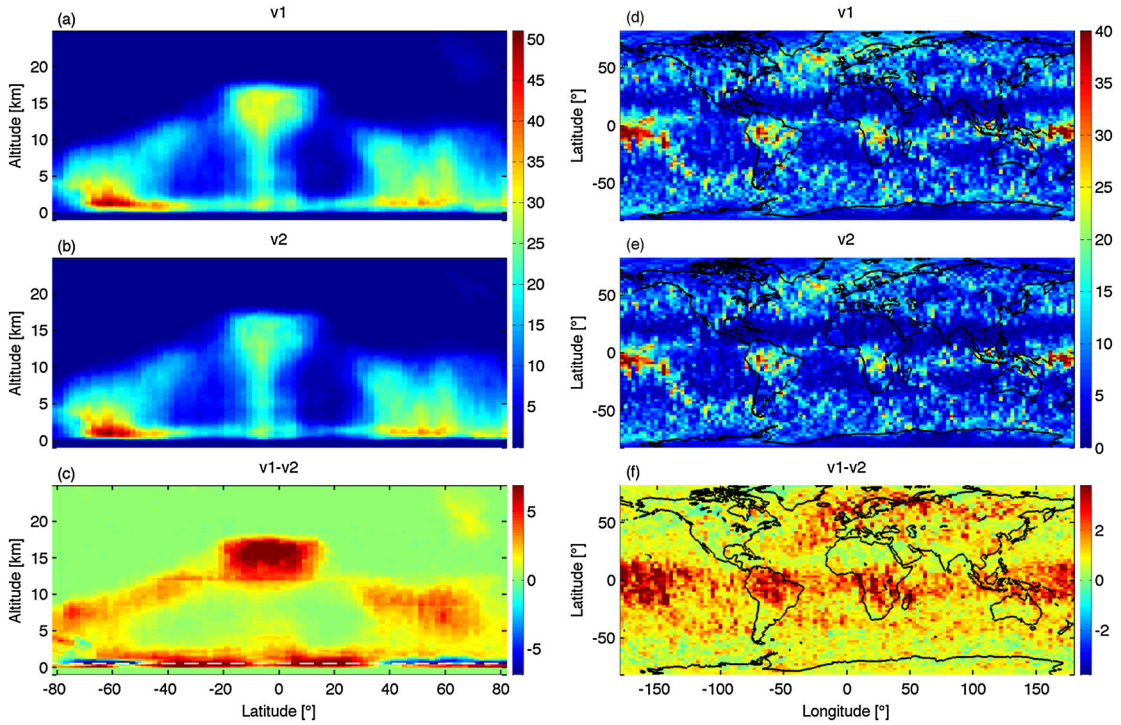


**Figure 10.** Comparison of rain or cloud occurrence in v1 and v2, defined as the number of pixels classified as clouds or rain divided by total number of pixels in each bin multiplied by 100. (a) Cloud or rain occurrence with respect to latitude and altitude for v1. (b) Same as Figure 10a but for v2. (c) The difference between Figures 10a and 10b with a white dashed line at 500 m altitude. (d) Same as Figure 10a but as a function of latitude and longitude. (e) Same as Figure 10d but for v2. (f) The difference between Figures 10e and 10f.

regions. The cloud or rain occurrence is calculated as the number of pixels classified as cloud or rain divided by the total number of pixels. The black line is the v1 distribution and the gray line the v2 distribution.

[41] In order to quantify the differences between the two classifications, the contingency table in Table 4 reports the number of pixels agreeing and disagreeing between the two versions. The lines and columns correspond to the pixels classified in v1 and v2, respectively. It is simplified in order to have the two classifications comparable. DARDAR v2 ice, low depolarization ice, top of convective clouds, and ice in high concentration pixels are all grouped in "Ice." Warm rain, cold rain, and mix of rain with liquid clouds are grouped in "Rain." The clutter pixels are included in "surface or subsurface" class, and finally the "lidar extinguished" and "lidar attenuated" grouped in "Unknown." At the end of each line and column, we give the total number of pixels attributed to the corresponding class in v1 and v2 and the agreement level between the two classifications. For instance in the "Ice" line, the total number of pixels classified as ice in v1 is 930,574. Of these pixels, 762,813 are also classified as ice in v2, which corresponds to an accordance of 82%, but 142,439 are classified as clear sky in v2, which corresponds to an disagreement of 15%. Such a disagreement is also apparent in Figure 7, clearly showing that on average DARDAR v1 includes more pixels in the classification than DARDAR v2. The occurrence differences reach 5% or more at low altitudes (below 2 km) in the tropics (Figure 7a), at high altitudes (above 7 km) in the middle northern latitudes (Figure 7b), and even reach 10% in the stratosphere in the South Pole (Figure 7e). Occurrence differences observed above 5 km are due to the block effect of the VFM; we have shown in section 2.2 that the v1 lidar mask includes, on average, more pixels than v2. The block effect is very well illustrated in Figure 8: Figures 8a and 8b are, respectively, the CPR reflectivity and the CALIOP backscatter in the South Pole, and Figures 8c and 8d are, respectively, the corresponding DARDAR v1 and v2 classifications. The stratospheric cloud observed between –81° and –77° in v1 encompasses more pixels than in v2 and has square contours. This is in agreement with the contingency table that indicates that 47% of stratospheric pixels in v1 are actually classified as clear sky in v2.

[42] As said in section 2.3, in v1, if a cloud and the clutter have common boundary, then all pixels below the boundary

**Table 5.** Moments of the Differences in Distribution of Cloud and Rain Occurrence Between DARDAR v1 and DARDAR v2 Shown in Figure 10

| – | Latitude-Altitude | Longitude-Latitude |
|---|---|---|
| Mean | 1.11% | 1.11% |
| Standard deviation | 1.85% | 0.81% |
| Maximum | 13.67% | 6.06% |
| Minimum | –16.15% | –0.76% |

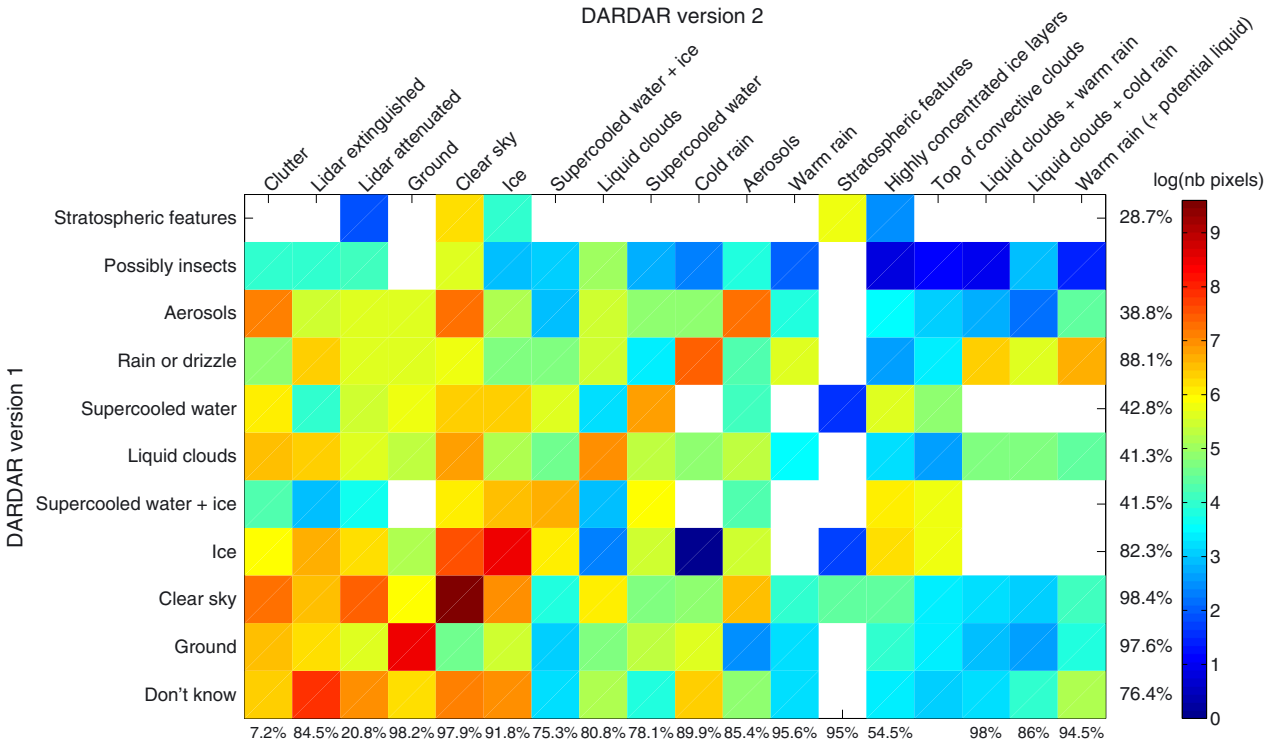


**Figure 11.** Contingency matrix of the two DARDAR versions using all available granules in January, February, and March 2010. The rows correspond to the classes in DARDAR v1 and the columns to the classes in DARDAR v2. The accordance percentage between v1 and v2 is given at the end of each row and column. The matrix gives an idea of the number of pixels dispatched into v2 classes which were originally classified as a particular type in v1. Each box is colored according to the logarithm of the number of pixels found in both the v1 and v2 classes. White boxes mean that there is no pixel mix-up between the two classes.

are given the same classification as the pixels above the boundary. This is not done in v2 because we cannot tell if liquid and ice clouds are precipitating or not, so we cannot confidently extend them to the ground without reliable reflectivity. Cold rain is the only hydrometeor that we extend to the ground even with contaminated radar reflectivity. An example of these differences is illustrated in Figure 8. In the descending pass around –60°, v2 reports some rain where, in v1, it is undefined because, in this region v1 has no common boundary with the clutter. In the ascending pass around –60°, v1 reports some ice below 1 km where, in v2, it is undefined. In this region, features in v1 have a few common boundaries with the clutter so v1 assigns as ice some square areas even if the reflectivity is obviously contaminated by clutter ($Ze \geq 15$ dBZ). Note that in warmer regions it happens with liquid clouds instead of ice. This effect can also be seen in the contingency table indicating an agreement of 65% for the "unknown" v1 class, but 4% of "unknown" v1 pixels are classified as rain in v2. Therefore, at low altitude (below 1.2 km), v2 could report more rain than v1 but v1 more ice and liquid clouds than v2.

[43] The differences observed in Figure 7a below 5 km altitude can be explained by the amount of liquid clouds reported in v1. In Figure 9c (same as Figure 8c but for the tropics), there are some artifacts in the detection of liquid clouds between aerosol areas at low altitudes between –25° and –16° and between 9° and 13° in the ascending pass. To a lesser extent in this granule, it appears as well in the descending passes. These cloud features are not realistic considering their shapes and the absence of strong lidar backscatter. These artifacts come from the fact that v1 assigned as liquid clouds the pixels classified as "aerosols none" and "clouds none" in the VFM. These pixels are usually not even included in the v2 lidar mask. This misclassification can be seen in the contingency table showing that there is only an accordance of 33% for the liquid clouds of v1. Indeed, 34.5% of liquid cloud pixels from v1 are actually classified as clear sky in v2, and 12.5% and 13.5% are classified as unknown and subsurface, respectively (remember that the v2 clutter is included in the subsurface in the contingency table). The low-altitude tropics are the regions where aerosols are mostly encountered; this is why this region has the largest differences in cloud or rain occurrence.

### 4.2. Comparison of the Two Classifications During Winter 2010

#### 4.2.1. Occurrences Comparison

[44] Figures 10a, 10b, and 10c show the clouds or rain occurrence distributions as a function of latitude and altitude for v1, v2, and the difference between v1 and v2, respectively, for granules of the winter 2010. Figures 10d, 10e, and 10f show the same occurrence as a function of longitude and latitude. The mean, standard deviation, maximum, and minimum of the distribution of the differences between v1 and

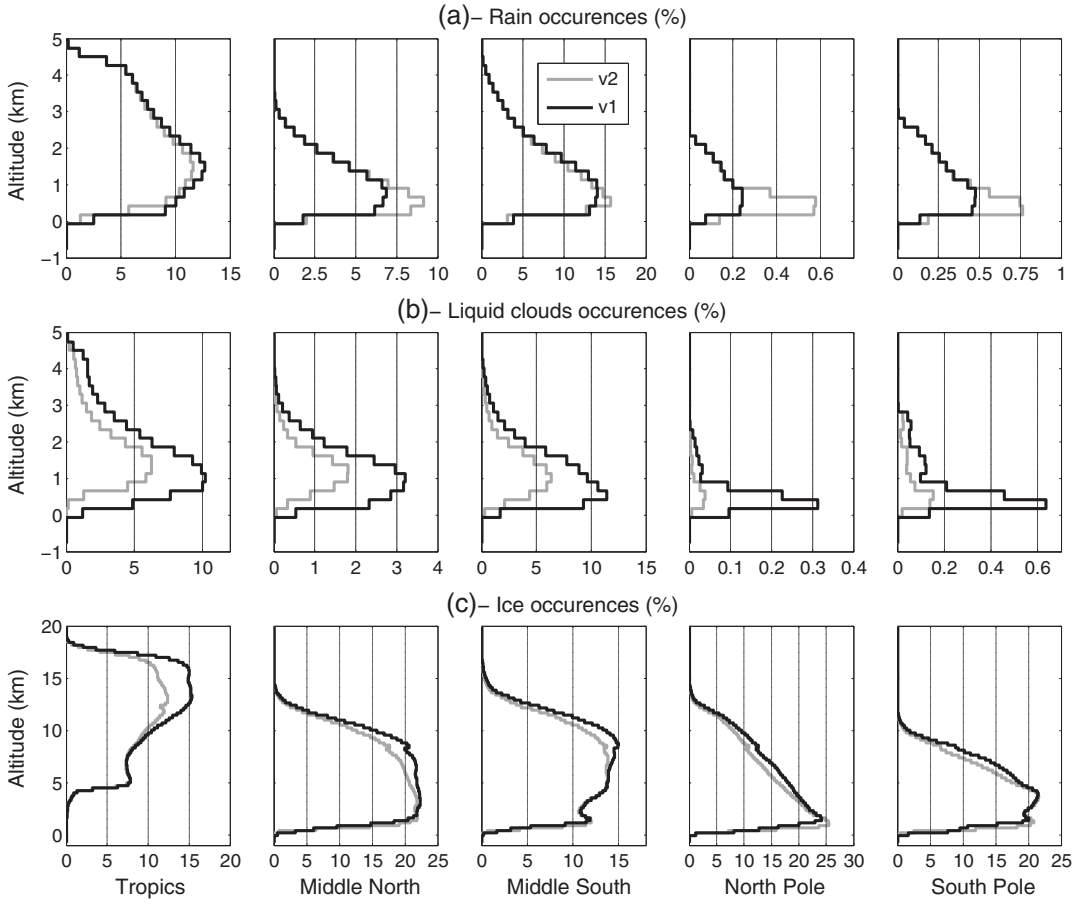


**Figure 12.** Histogram with respect to altitude of (a) rain, (b) liquid clouds, and (c) ice occurrence in different regions for the two DARDAR classifications in winter 2010.

v2 are listed in Table 5. Figure 11 is the contingency table for these data displayed with colors corresponding to the logarithm of the number of pixels in each grid box. The matrix presents all the classes from v2 (except low depolarization ice) in order to understand the impacts of the introduction of new classes in the classification. The colors help to visualize the correspondence between the two classifications and to quickly identify the classes between which there is the most confusion. The white boxes correspond to the classes for which there is no confused pixel.

[45] Figures 10a and 10b show that clouds and rain are distributed according to latitude and altitude. Figure 10c and Table 5 show that the differences between the two versions can reach 16% in some areas. This represents a significant difference when it comes to evaluating general circulation models (GCMs). Figures 10d and 10e show some geographical dependence. Most clouds or rain are located in the tropics, in the Northern Atlantic, and in Northern Europe, and this is where the largest differences are consequently observed in Figure 10f (not more than 6% according to Table 5).

[46] Figure 10c shows an almost continuous red area below 500 m (white dashed line), indicating that v1 occurrences are larger by 5–6% than v2 occurrences. For slightly higher altitudes, between 500 m and 2 km, red still predominates in the tropics and middle latitudes, while in the poles v2 occurrences are larger by 5–6% than v1 occurrences. This observation is consistent with the difference in the way clutter is treated in v1 and v2, as discussed in section 4.1. Differences are more easily quantifiable in Figures 12a, 12b, and 12c that show the rain, liquid clouds, and ice occurrence, respectively, in DARDAR v1 in black and v2 in gray for different latitude regions. For rain above 1.2 km, where clutter treatment has no more effect, there is almost no difference between the two versions, but below 1.2 km, v2 reports more rain than v1 (except in the tropics). For liquid clouds, the largest differences are also located below 1.2 km where v1 reports more liquid clouds than v2.

[47] Above this limit the differences are explained by the false liquid cloud detection in aerosol areas, discussed previously. The contingency table tells us that v1 "liquid clouds" pixels are dispatched into several classes in v2. First of all, 12.8% of these pixels are classified as clutter in v2 because liquid clouds in v1 are extended to the ground where v2 reports nothing but ground clutter. Secondly, 11.7% of them are classified as extinguished lidar in v2. This happens when spurious detection is found in the middle of an extinction area (such cases were observed but are not shown here). Finally, as expected, 28.1% of them are classified as clear sky in v2.

[48] In Figure 10c at high altitudes in the tropics, the differences reach more than 15% due to v1 being less restrictive on cloud pixel detection than v2 and because of the block effect (see section 2.2). Note in Figure 11 that the v2 "clear

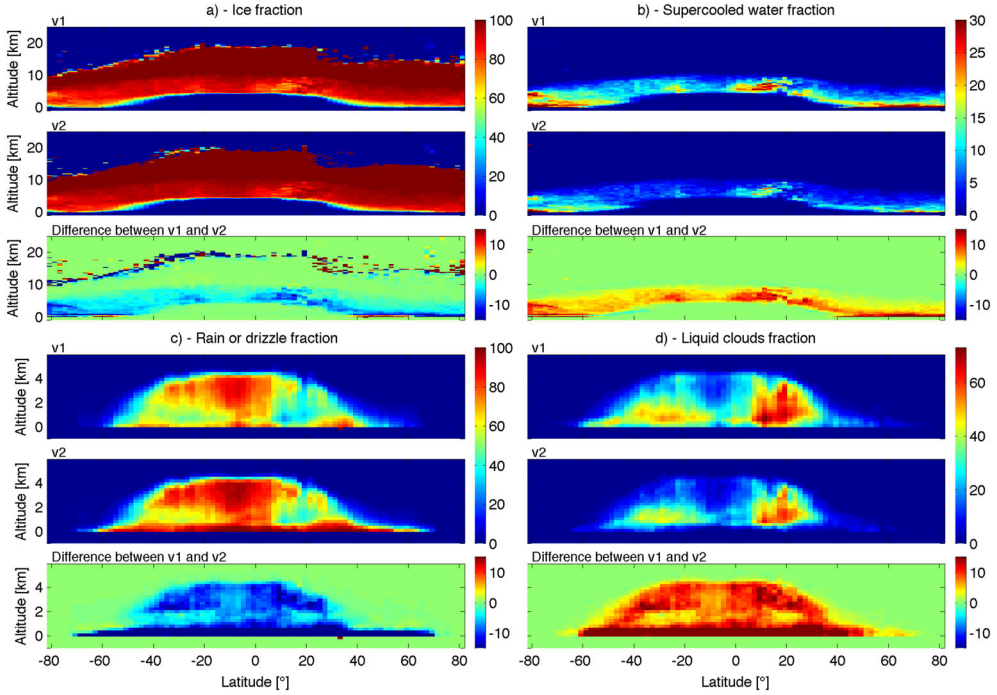


**Figure 13.** Comparison of the distribution of atmospheric constituents, with respect to altitude and latitude, for DARDAR v1 and v2. (a) The distribution of ice fraction calculated as the number of pixels classified as ice divided by the number of pixels classified as cloud or rain in the same bin. The top plot is for v1, the middle plot is for v2, and the bottom plot shows the difference in fractions between the two versions. (b) Same as Figure 13a but for supercooled water (mixed with ice or not) fraction. (c) Same as Figure 13a but for rain or drizzle fraction. (d) Same as Figure 13a but for liquid clouds fraction.

sky" pixels are dispatched to many classes in v1, such as ice, liquid clouds, aerosols, and stratospheric features. Discrepancies between the v1 and v2 lidar masks make the v1 accordance for those classes not very good: the v1 stratospheric accordance in only 28.7%, the remaining pixels are categorized mainly as clear sky and ice in v2. For liquid clouds, there are almost as many pixels classified as clear sky as are classified as liquid clouds in v2. Fifteen percent of v1 ice pixels are classified as clear sky in v2. Figure 12c also shows that there is quite a good match between the two versions below 8 km in the tropics and below 5 or 6 km in other regions. This corresponds to areas where ice is mainly detected by radar; we showed earlier that radar masks on v1 and v2 are almost identical.

#### 4.2.2. Phase Fractions Comparison

[49] Figure 13 presents the distribution of ice, rain, supercooled water (mixed with ice or not), and liquid clouds fractions as a function of altitude and latitude. The fraction is defined as the number of pixels classified as a certain type of hydrometeor divided by the number of pixels classified as cloud or rain. It represents the chance that a pixel will belong to a class when detected by the radar and/or the lidar. For instance, an ice fraction of 100% means that, in the considered bin, the only hydrometeor to be found is ice. Comparing the fractions helps to identify the discrepancies between classes and to identify the locations where different hydrometeors coexist.

[50] It is clear from Figures 13a and 13b that there is a mix-up between ice and supercooled water. Indeed, the increase in ice fraction in v2 (higher fraction v2 by up to 15%) in Figure 13a perfectly matches the decrease in supercooled water fraction (lower fraction in v2 by up to 15%) in Figure 13b. This means that v1 is more likely to assign the target pixels to supercooled water than v2. This is verified by the contingency table in Figure 11 (numbers not displayed in the figure) where 20.5% of the pixels classified as supercooled water in v1 are classified as ice in v2. This is because v1 sometimes includes an additional pixel above and below the actual layer of strong backscatter (see discussion in section 3.1).

[51] The differences observed along the tropopause in Figure 13a correspond to the mix-up between stratospheric and tropospheric pixels.

[52] Figure 13c shows that, in many areas, the fraction of rain or drizzle is larger by 10 to 15% in v2 than in v1, while we observe the opposite for liquid clouds in Figure 13d. Similarly to ice and supercooled water, the changes between v1 and v2 in rain and liquid clouds match each other. Rain fraction in v2 includes the fractions of cold rain, warm rain, and any kind of rain mixed with liquid clouds. The contingency matrix confirms, as expected, the mix-up between liquid clouds in v1 and liquid clouds mixed with rain in v2. When grouping all rain classes from v2, we have 91.5% agreement with v1 pixels. Of rain pixels in v2, 0.4% are classified as liquid clouds in v1 and the other 7% as unknown, clear sky, or surface, but these latter do not play a part in the fraction computation. Therefore, we see that a small mix-up of 0.4% can represent quite a big difference in fractions: the maximum differences (not displayed in Figure 13c for visibility reasons) reach 80% in low altitudes (below 1 km).

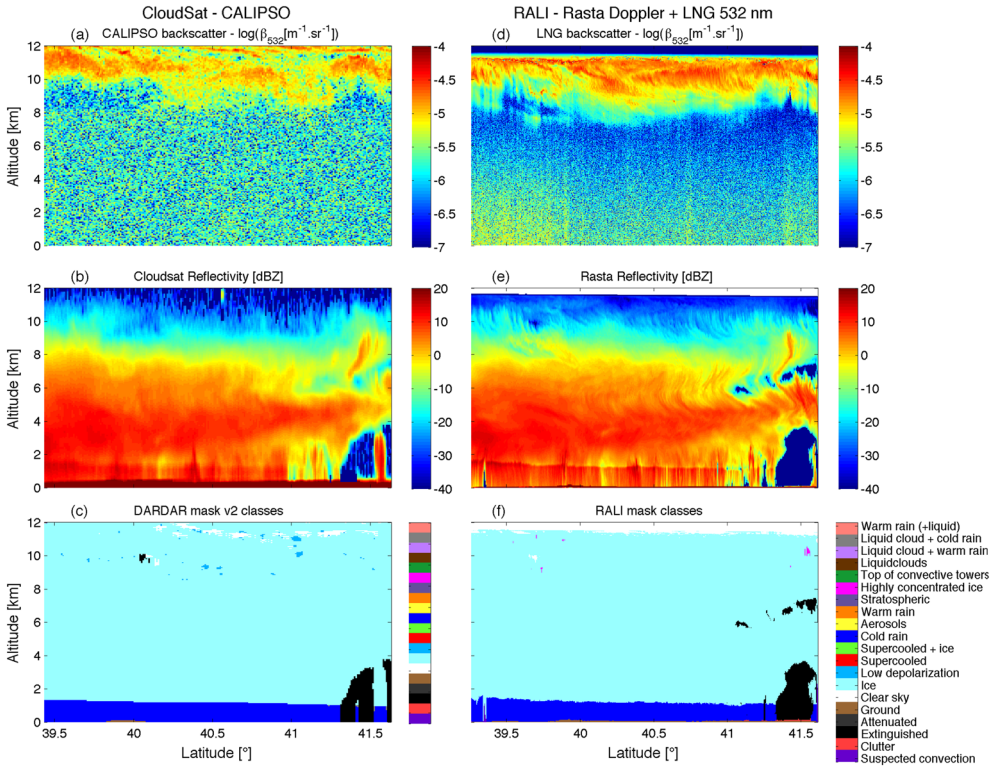


**Figure 14.** Comparison of DARDAR v2 and RALI classification during the LNG-CALIPSO campaign on 29 November 2010 (Flight 33). (a) CALIOP backscatter $\beta_{532}[\mathrm{m}^{-1}\,\mathrm{sr}^{-1}]$, (b) CloudSat reflectivity Ze [dBZ], (c) classification result from DARDAR v2 algorithm, (d) LNG backscatter $\beta_{532}[\mathrm{m}^{-1}\,\mathrm{sr}^{-1}]$, (e) RASTA reflectivity Z [dBZ], and (f) classification result from RALI algorithm.

Rain fraction in v2 reaches 100% below 1 km because, as detailed previously, it is the only hydrometeor which can be assigned so close to the surface in regions where it is more than 0°C. In v1, some of the clutter contaminated pixels were assigned as liquid clouds or ice, hence the lower fraction.

## 5. Adaptation of the DARDAR v2 Algorithm to Airborne RALI Data

### 5.1. RALI Missions and Data Sets

[53] RALI is an instrumentation project devoted to the characterization of microphysical, macrophysical, radiative, and dynamical properties of clouds, aerosols, and convection [*Protat et al.*, 2004]. It consists of an airborne platform (either a Falcon 20 or an ATR-42 aircraft) combining RASTA (Radar System Airborne), a 95 GHz Doppler cloud radar, and LNG (Leandre New Generation), a triple-wavelength (355 nm, 532 nm, and 1064 nm) dual-polarization lidar with HSR capabilities at 355 nm. The HSR gives the opportunity to separate molecular from particle return in the lidar signal and therefore to get a direct measurement of extinction [*Bruneau and Pelon*, 2003]. For more details about the RALI project, see *Protat et al.* [2004] and *Delanoë et al.* [2013].

[54] Since the launch of the A-Train satellites, several RALI campaigns were conducted (http://rali.projet.latmos.ipsl.fr). The campaigns where both radar and lidar data were acquired are as follows:

[55] 1. CIRCLE II (Cirrus Cloud Experiment II) in May 2007 in France and Germany. The mission was designed for satellite validation and study of cirrus clouds properties.

[56] 2. EUCAARI (European integrated project on Aerosol Cloud Climate and Air Quality Interactions) in Spring 2007 in the Netherlands. The mission's scientific objectives were aerosol, cloud, climate, and air quality interaction studies.

[57] 3. POLARCAT (Polar Study using Aircraft, Remote Sensing, Surface Measurements, and Models of Climate, Chemistry, Aerosols, and Transport) [*Stohl et al.*, 2010] in Spring 2008 in northern Scandinavia dedicated to the investigation of arctic processes, including cloud processes [*Delanoë et al.*, 2013].

[58] 4. LNG-CALIPSO (Leandre New Generation-CALIPSO) in Autumn 2010 over the Atlantic for CALIPSO validation and LNG HSR tests.

[59] During the CIRCLE II, POLARCAT, and LNG-CALIPSO missions, several A-Train overpasses were carried out. As the RALI platform carries a 95 GHz radar and a 532 nm lidar, the data collected during these overpasses were very useful to check the performance of CloudSat and CALIOP instruments as well as the new version of the DARDAR classification algorithm. Moreover, during the LNG-CALIPSO mission, HSR lidar data at 355 nm during

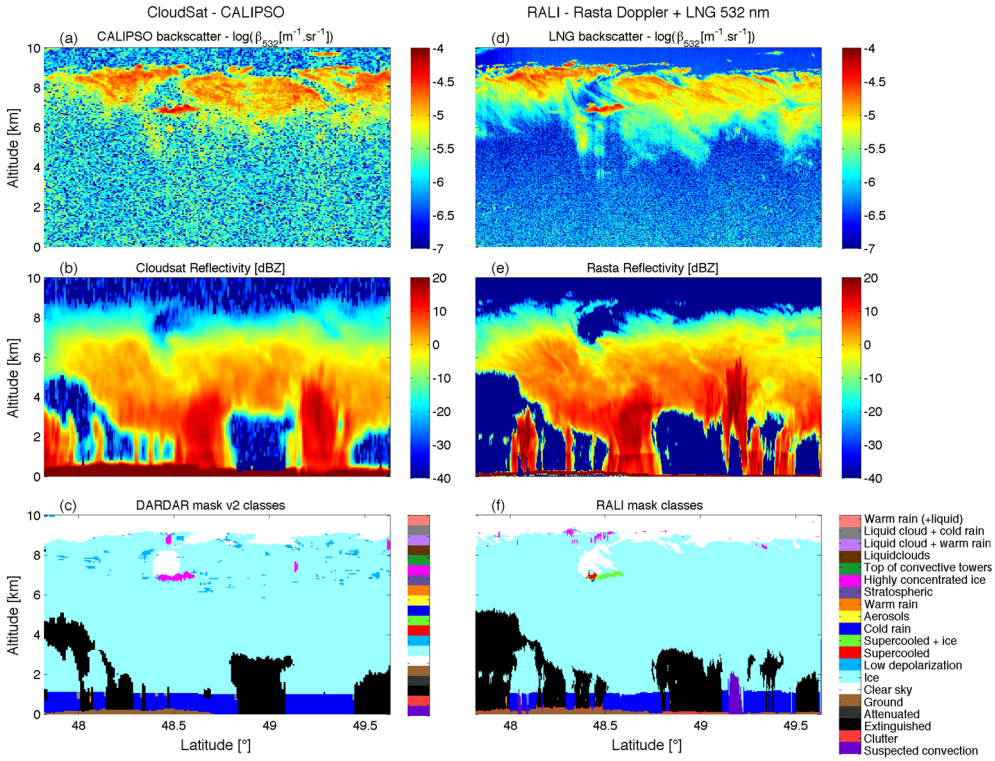


**Figure 15.** Comparison of DARDAR v2 and RALI classification during the LNG-CALIPSO campaign on 4 December 2010 (Flight 36). (a) CALIOP backscatter $\beta_{532}$[m$^{-1}$ sr$^{-1}$], (b) CloudSat reflectivity Ze [dBZ], (c) classification result from DARDAR v2 algorithm, (d) LNG backscatter $\beta_{532}$[m$^{-1}$ sr$^{-1}$], (e) RASTA reflectivity Z [dBZ], and (f) classification result from RALI algorithm.

A-Train overpasses are available to evaluate the CALIPSO extinction retrieval algorithm, which will be the subject of future work.

### 5.2. A-Train/RALI Overpasses Case Study

[60] The comparison of airborne and spaceborne classifications allows for an investigation of errors due to the coarser resolution of the spaceborne measurements as compared to RALI. The original resolution of the RALI data are 15 m vertical and 30 to 100 m horizontal resolution for LNG and 60 m vertical resolution for RASTA with a sensitivity down to –37 dBZ. These data, interpolated on a 60 m vertical resolution and 3 s horizontal resolution grid, reveal more details of the cloud structures than satellite data. The LNG lidar data are far less noisy than those from CALIOP. This difference in noise is due to the smaller field of view of LNG which allows fewer solar photons to corrupt the signal. Therefore, for the lidar mask creation, LNG needs no different treatment whether it is day or night. Moreover, LNG is also less affected by multiple scattering than CALIOP.

[61] For the comparison of airborne and satellite classifications, we have adapted the DARDAR v2 algorithm to RALI data on A-Train overpasses. Results from DARDAR and RALI are then compared in order to identify the differences between the two classifications and understand their consequences in our ability to classify the different types of hydrometeors.

[62] Figure 14 presents satellite data with DARDAR v2 classification and airborne data with its corresponding classification during the LNG-CALIPSO campaign on 29 November 2010 (Flight 33). This overpass gives a good example of melting layer detection. In RALI the melting layer is located with Doppler signal, whereas in DARDAR, ECMWF AUX data, whose original vertical resolution is 240 m, are used. Figures 14c and 14f show that melting layers from both satellite and airborne classifications are quite similar. Assuming that the melting layer obtained with Doppler measurements is accurate, we find a height root mean square error (RMSE) for the ECMWF 0°C isotherm of 57 m and a bias of 25 m.

[63] Figure 15 gives another example of A-Train overpass on 4 December 2010 (Flight 36). On this example, we have a RMSE of 116 m and a bias of –48 m, with the largest differences about ±300 m.

[64] Comparing melting layers in DARDAR and RALI classifications gives an idea of how precisely DARDAR v2 locates the melting layer using ECMWF wet bulb temperature. These examples show that if the rain is stratiform, there is a very good correspondence (error smaller than a gate of 60 m), but when there is more convection the differences can reach 300 m, which is quite significant but still smaller than the native vertical resolution of CloudSat.

[65] *Mittermaier and Illingworth* [2002] ran the same kind of comparison but with a vertically pointing ground-based radar at 94 GHz in Chilbolton. The ECMWF wet bulb 0°C isotherm is compared to the observed bright band height which is defined as the height of the step increase in radar reflectivity. The authors found, with a much larger data set, a RMSE of 316 m and a bias of 58 m above the observed bright

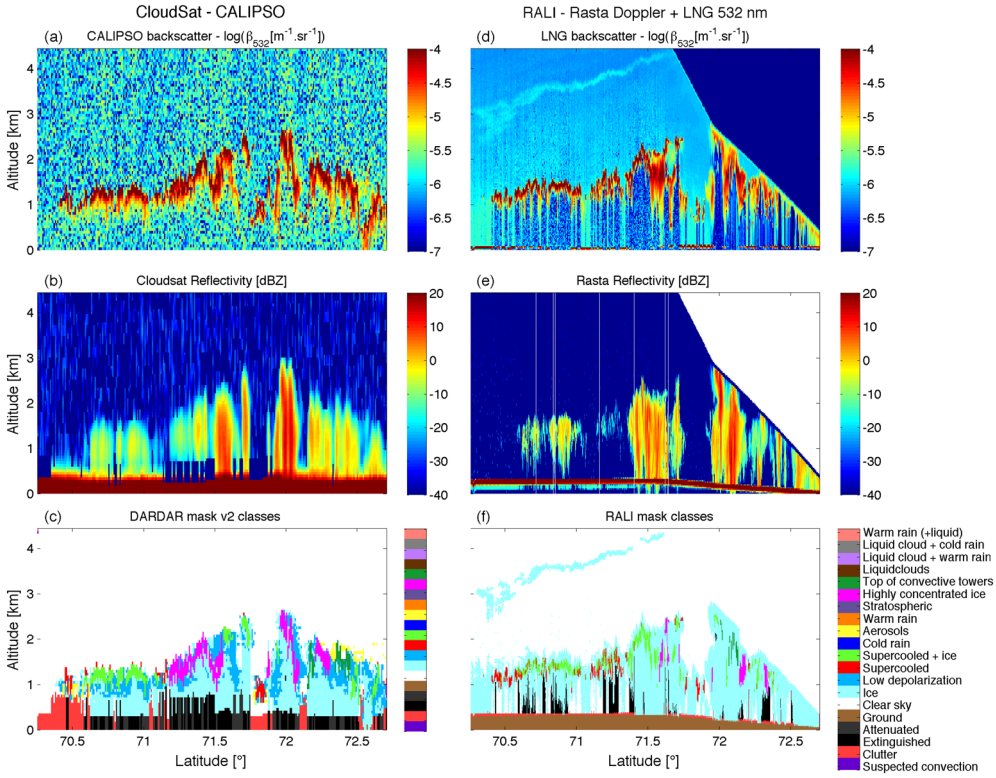


**Figure 16.** Comparison of DARDAR v2 and RALI classification during the POLARCAT campaign on 10 April 2008 (Flight 34). (a) CALIOP backscatter $\beta_{532}$[m$^{-1}$ sr$^{-1}$], (b) CloudSat reflectivity Ze [dBZ], (c) classification result from DARDAR v2 algorithm, (d) LNG backscatter $\beta_{532}$[m$^{-1}$ sr$^{-1}$], (e) RASTA reflectivity Z [dBZ], and (f) classification result from RALI algorithm.

band. Our study gives slightly different results of RMSE but about the same order of magnitude; more RALI case studies would be useful to compare [*Mittermaier and Illingworth*, 2002] results with ours. We must also remember that the data used in *Mittermaier and Illingworth* [2002] are collected from the ground, while RALI data are obtained from an aircraft resulting in different viewing geometries. Furthermore, we use the Doppler signal to identify the melting layer, whereas *Mittermaier and Illingworth* [2002] used reflectivity measurements. The two approaches are slightly different since the Doppler signal indicates the altitude where the particles start to fall, whereas the step increase in radar reflectivity indicates the altitude where ice particles start to get coated in liquid water. Doppler signal is more adapted to melting layer detection, especially with a 95 GHz radar where the bright band can be barely noticeable. Note that the differences found can also be explained by ECMWF model improvements within the last decade.

[66] Moreover, areas of strong convection can be observed in RALI but unfortunately not in satellite data. In the RALI classification a class called "Suspected convection" is added. Indeed, it is a class derived from the lack of RASTA data. In these cases, RASTA is extinguished (even the ground is missing in the signal), and usually the Doppler signal indicates updraft and precipitation areas nearby each other. It is very difficult to create a convenient class since in convective clouds, different hydrometeors are mixed together. Updrafts drag liquid droplets above the 0°C isotherm, and, when they weaken, the droplets start to precipitate again, hence the confused Doppler signal. This is clearly seen during the Flight 36 of the LNG-CALIPSO mission in Figure 15 at 49.2° and 48.1°. In Figure 15e, at 49.2° between 3 and 4 km, the RASTA signal is very strong but quickly attenuated, whereas the CloudSat reflectivity in Figure 15b still reaches 10 dBZ. In this region, the Doppler signal (not displayed here) shows a situation of both updraft and precipitation. Such phenomenon is described in *Battaglia et al.* [2007], where multiple scattering (MS) enhancement (difference between multiple- and single-scattering reflectivity) from CloudSat and airborne radar are compared. The authors show that the MS enhancement is lower than 3 dB in the airborne configuration, whereas it can reach very high values in the spaceborne configuration when passing through areas of strong content of hydrometeors. This can explain the differences observed in Figure 15, but we must also remember that CloudSat's sensitivity does not drop much with range contrary to RASTA. Without Doppler we can only rely on ECMWF, which gives no information on updrafts. The use of Doppler therefore helps to locate the melting layer and also the convection areas.

[67] Comparing the classifications from airborne and space instruments is also interesting regarding the location and classification of strong backscatter layers. Figures 15 and 16 give examples of such layers. The algorithm stays the same for both the airborne or spaceborne lidar data since both lidar operate at the same wavelength, 532 nm, but ever so, the classification for these layers differs. For instance,

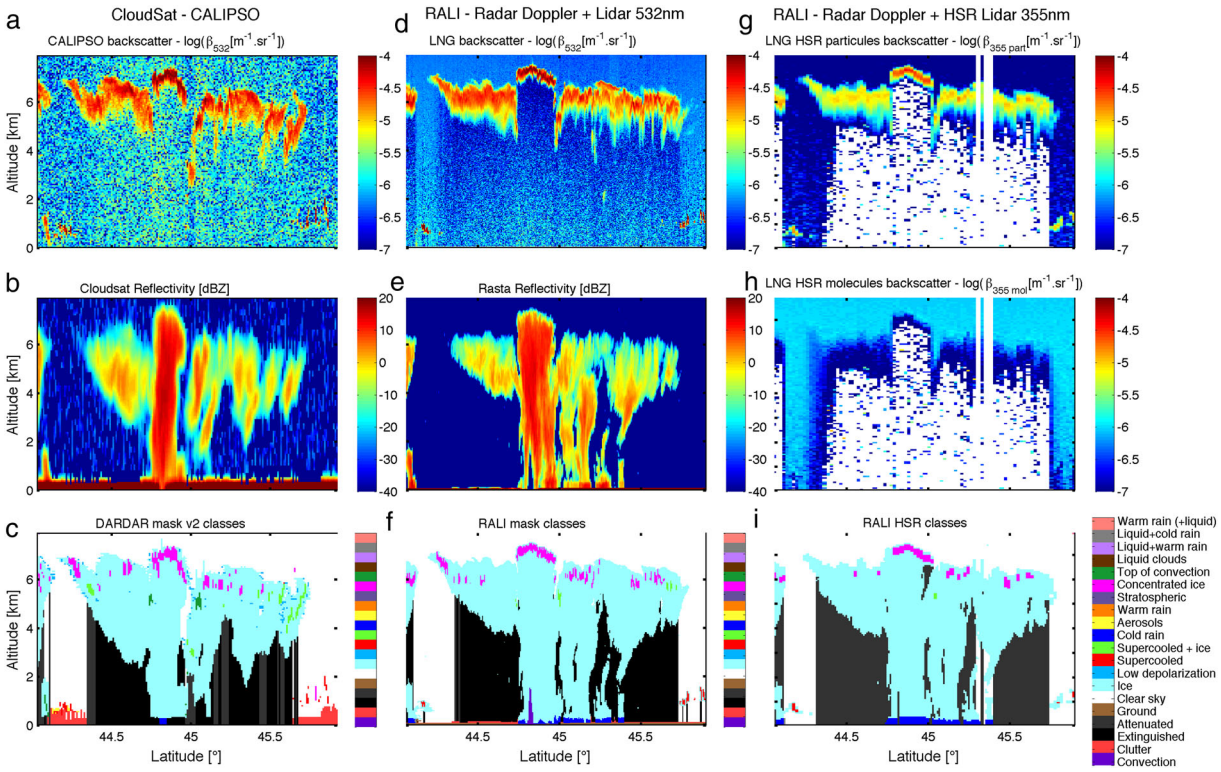


**Figure 17.** Results of the RALI mask and comparison with DARDAR masks. (a to c) Spaceborne data and DARDAR v2 classification. (d to f) RALI data with LNG 532 nm Doppler and resulting classification. (g to i) RALI data with HSR LNG 355 nm and resulting classification.

in Figure 15, the strong backscatter layer found at 7 km and 48.6° is classified as ice in high concentration in DARDAR and as a mix of supercooled water and ice in RALI. Similarly, Figure 16 shows an example of a layer classified as ice in high concentration in DARDAR and as a mix of supercooled water and ice in RALI. This difference is due to the thickness of the layer. The comparison between CALIOP and LNG data shows that the CALIOP layer looks much thicker than the LNG one, and this might be because of multiple scattering. Since the algorithm relies on a thickness threshold to separate ice and liquid, the results can be very sensitive to a small variation of layer thickness.

[68] CALIOP and LNG data in Figure 16 show that CALIOP data are quite noisy and do not reveal the cloud running from 3 km at 70.5° to 4.5 km at 71.5°. For the moment RALI classifies this as ice cloud but it could be aerosols. Similarly, the low level cloud located around 70.3° is probably aerosols, but because the RALI algorithm does not have a method to distinguish clouds from aerosols, we leave it as clouds for now. This tells us that RALI is able to detect clouds with signal down to $\beta_{532} = \exp(-5.9)\,m^{-1}\,sr^{-1}$ in a noise signal of $\beta_{532} = \exp(-6.2)\,m^{-1}\,sr^{-1}$, whereas in CALIOP the noise lies around $\beta_{532} = \exp(-5.7)\,m^{-1}\,sr^{-1}$ and therefore misses such optically thin clouds or aerosols layers.

[69] We have only been able to run this kind of comparison on the few RALI cases where A-Train overpasses were available. This study, therefore, does not constitute a proper validation of the DARDAR v2 algorithm, but it does help to identify the classes where DARDAR classification should be taken with caution.

### 5.3. Adaptation of the Algorithm to RALI Data in Preparation for EarthCare

[70] RALI is the perfect instrument to prepare for the transition from CloudSat-CALIPSO products to EarthCare. Indeed, RALI carries the same active instruments as in each of the two spaceborne systems. RASTA is a Doppler 95 GHz radar equivalent to the 95 GHz Cloud Profiling Radar on CloudSat and the 95 GHz Doppler CPR on EarthCare. LNG is a three-wavelength lidar (355 nm with HSR, 532 nm, and 1064 nm) like CALIOP (532 nm and 1064 nm) and like EarthCare (355 nm with HSR).

[71] The first step in the creation of the EarthCARE classification is to adapt DARDAR v2 to airborne data (see previous section). The second step which we detail in this section is to adapt the airborne RALI algorithm to the HSR 355 nm lidar in order to have an algorithm almost ready to use when EarthCare data are available. The only modification that has to be done here lies in the lidar detection and thresholding at 355 nm. A comparison of $\beta_{532}$ versus $\beta_{355}$ from the LNG lidar (not shown here) shows that the corresponding threshold for the selection of strong backscatter layers at 532 nm $\beta_{532} > 2.10^{-5}\,m^{-1}\,sr^{-1}$ is $\beta_{355} > 1.10^{-5}\,m^{-1}\,sr^{-1}$.

[72] Figure 17 presents the two steps of preparation for EarthCare for flight 35 on 2 December 2010. On the left column (Figures 17a, 17b, and 17c), we present CALIPSO and CloudSat profiles on the overpass and the resulting

DARDAR v2 classification. The middle column shows RALI data with LNG at 532 nm (Figure 17d), RASTA (Figure 17e), and the resulting RALI classification (Figure 17f). The right column shows RALI data with HSR capabilities at 355 nm with particle return (Figure 17g), molecular return (Figure 17h), and the resulting classification (Figure 17i). The horizontal resolution is lower when using HSR data because it requires temporal averaging, but the vertical resolution is still 60 m as for the spaceborne data. HSR capabilities are revealed useful to create the lidar mask directly from the particle returns. The resulting HSR RALI classification shown in Figure 17i shows good agreement with the RALI classification in Figure 17f. Nevertheless, more LNG HSR data would be needed to test the algorithm more thoroughly. HSR data could also be further investigated to develop a method to discriminate aerosols from clouds using the depolarization and the extinction-to-backscatter ratio.

## 6. Conclusion and Perspectives

[73] In this paper, we have detailed the method to create the new DARDAR classification version from CloudSat and CALIPSO profiles. It represents a step toward EarthCare as it does not rely on NASA official Level 2 products except to distinguish clouds from aerosols. Moreover, it is improved from the first DARDAR version in the sense that it is less affected by the lidar block effect and false detection of liquid clouds in the lower troposphere. It is believed that the amount of clouds reported in DARDAR v2 is closer to reality and hence better for evaluating GCMs.

[74] The DARDAR v2 algorithm also has the advantage that it can be easily transposed to either RALI data with lidar at 532 nm and Doppler radar or ground-based radar and lidar. The results from the comparison between DARDAR v2 and RALI classifications during overpasses on the POLARCAT and LNG-CALIPSO campaigns revealed that ice in high concentration is to be taken with caution and that future work should take into account the effects of multiple scattering. They also tell us that the melting layer is locally precise to $\pm 300$ m, especially in the cases where convection lies in the rain structure, but globally the differences are expected to be around $\pm 100$ m. In stratiform cases the ECMWF estimate is quite reliable. The Doppler data are very useful to validate and quantify the errors in the ECMWF 0°C isotherm and to locate strong convection areas. We have also seen that the DARDAR classification can miss some clouds (or aerosols) because of noise in the CALIOP data.

[75] Finally, we have shown that the RALI classification algorithm can be easily transposed to RALI data with HSRL at 355 nm. The results from the three classification algorithms tested on the overpass acquired during the Flight 35 of LNG-CALIPSO campaign on 2 December 2010 are quite similar. This is very encouraging and proves that it is sensible to use RALI data to prepare for the transition from CloudSat and CALIPSO to EarthCare.

[76] The use of HSR lidar observations also seems to be very promising, and future work regarding the DARDAR product will consist of using it to distinguish aerosols from cloud.

[77] **Acknowledgments.** Marie Ceccaldi's research is funded by CNES and ACRI-ST. Julien Delanoë's research is partly funded by CNES. We thank the engineers and technicians who are continuously working on the LNG and RASTA projects at DT/INSU and LATMOS. Spaceborne data were provided by NASA/CNES, and we thank the ICARE Data and Services Center (http://www.icare-lille1.fr) for providing access to the data used in this study.

## References

Battaglia, A., M. O. Ajewole, and C. Simmer (2007), Evaluation of radar multiple scattering effects in CloudSat configuration, *Atmos. Chem. and Phys.*, *7*, 1719–1730, doi:10.5194/acp-7-1719-2007.

Bruneau, D., and J. Pelon (2003), Simultaneous measurements of particle backscattering and extinction coefficients and wind velocity by lidar with a mach-zehnder interferometer: Principle of operation and performance assessment, *Appl. Optics*, *42*(6), 1101–1114.

Delanoë, J., and R. J. Hogan (2008), A variational scheme for retrieving ice cloud properties from combined radar, lidar and infrared radiometer, *J. Geophys. Res.*, *113*, D07204, doi:10.1029/2007JD009000.

Delanoë, J., and R. J. Hogan (2010), Combined CloudSat-CALIPSO-MODIS retrievals of the properties of ice clouds, *J. Geophys. Res.*, *115*, D00H29, doi:10.1029/2009JD012346.

Delanoë, J., R. J. Hogan, G. van Zadelhoff, and H. Barker, (2010), Radiative transfer modelling for Earth-CARE (RATEC), *Technical Report*, Univ. of Reading, Reading, U. K.

Delanoë, J., R. J. Hogan, R. M. Forbes, A. Bodas-Salcedo, and T. H. M. Stein (2011), Evaluation of ice cloud representation in the ECMWF and UK Met Office models using CloudSat and CALIPSO data, *Q. J. R. Meteorol. Soc.*, *137*, 2064–2078, doi:10.1002/qj.882.

Delanoë, J., A. Protat, O. Jourdan, J. Pelon, M. Papazzoni, R. Dupuy, J. F. Gayet, and C. Jouan (2013), Comparison of airborne in-situ, airborne radar-lidar, and spaceborne radar-lidar retrievals of polar ice cloud properties sampled during the POLARCAT Campaign, *J. Atmos. Oceanic Technol.*, *30*, 57–73, doi:10.1175/JTECH-D-11-00200.1.

Deng, M., G. Mace, Z. Wang, and H. Okamoto (2010), Tropical composition, cloud and climate coupling experiment validation for ice cloud profiling retrieval using CloudSat radar and CALIPSO lidar, *J. Geophys. Res.*, *115*, D00J15, doi:10.1029/2009JD013104.

Hogan, R. J., P. N. Francis, H. Flentje, A. J. Illingworth, M. Quante, and J. Pelon (2003), Characteristics of mixed-phase clouds: Part I. Lidar, radar and aircraft observations from CLARE '98, *Quart. J. Roy. Meteor. Soc.*, *129*, 2089–2116, doi:10.1256/rj.01.208.

Hogan, R. J., M. D. Behera, E. J. O'Connor, and A. J. Illingworth (2004), Estimate of the global distribution of stratiform supercooled liquid water clouds using the lite lidar, *Geophys. Res. Lett.*, *31*, L05106, doi:10.1029/2003GL018977.

Huang, Y., S. T. Siems, M. J. Manton, A. Protat, and J. Delanoë (2012), A study on the low-altitude clouds over the Southern Ocean using the DARDAR-MASK, *J. Geophys. Res.*, *117*, D18204, doi:10.1029/2012JD017800.

Jouan, C., E. Girard, J. Pelon, I. Gultepe, J. Delanoë, and J. P. Blanchet (2012), Characterization of arctic ice cloud properties observed during ISDAC, *J. Geophys. Res.*, *117*, D23207, doi:10.1029/2012JD017889.

Leon, D. C., Z. Wang, and D. Liu (2008), Climatology of drizzle in marine boundary layer clouds based on 1 year of data from CloudSat and CALIPSO, *J. Geophys. Res.*, *113*, D00A14, doi:10.1029/2008JD009835.

Liu, Y., B. Geerts, M. Miller, P. Daum, and R. McGraw (2008), Threshold radar reflectivity for drizzling clouds, *Geophys. Res. Lett.*, *35*(L03807), doi:10.1029/2007GL031201.

Marchand, R., G. G. Mace, T. Ackerman, and G. Stephens (2008), Hydrometeor detection using CloudSat—An Earth-orbiting 94 GHz cloud radar, *J. Atmos. Oceanic Technol.*, *25*, 519–533, doi:10.1175/2007JTECHA1006.1.

Mittermaier, M. P., and A. J. Illingworth (2002), Comparison of model-derived and radar-observed freezing level heights: Implications for vertical reflectivity profile correction schemes, *Q. J. R. Meteorol. Soc.*, *129* (587), 83–95, doi:10.1256/qj.02.19.

Okamoto, H., K. Sato, and Y. Hagihira (2010), Global analysis of ice microphysics from CloudSat and CALIPSO: Incorporation of specular reflection in lidar signals, *J. Geophys. Res.*, *115*, D22209, doi:10.1029/2009JD013383.

Protat, A., et al. (2004), Le projet rali: Etude des nuages faiblement précipitants par télédétection active, *Meteorologie*, *47*, 23–33.

Protat, A., D. Bouniol, J. Delanoë, P. T. May, A. Plana-Fattori, A. Hasson, E. J. O'Connor, U. Gorsdorf, and A. J. Heymsfield (2009), Assessment of CloudSat reflectivity measurements and ice cloud properties using ground-based and airborne cloud radar observations, *J. Atmos. Oceanic Technol.*, *26*, 1717–1741, doi:10.1175/2009JTECHA1246.1.

Reehorst, A., D. Brinker, M. Politovich, D. Serke, C. Ryerson, A. Pazmany, and F. Solheim (2008), Progress towards the remote sensing of aircraft

icing hazards, in *Remote Sensing Applications for Aviation Weather Hazard Detection and Decision Support, Proceedings of SPIE,* vol. 7088, edited by W. F. Feltz and J. J. Murray, SPIE, Bellingham, Wash.

Stein, T. H. M., D. J. Parker, J. Delanoë, N. S. Dixon, R. J. Hogan, P. Knippertz, R. I. Maidment, and J. H. Marsham (2011a), The vertical cloud structure of the West African monsoon: A 4 year climatology using CloudSat and CALIPSO, *J. Geophys. Res.*, *116*, D22205, doi:10.1029/2011JD016029.

Stein, T. M., J. Delanoë, and R. J. Hogan (2011b), A comparison among four different retrieval methods for ice-cloud properties using data from CloudSat, CALIPSO, and MODIS, *J. Appl. Meteorol. Climatology*, *50*, 1952–1969, doi:10.1175/2011JAMC2646.1.

Stephens, G. L. (2005), Cloud feedbacks in the climate system: A critical review, *J. Clim*, *18*, 237–273, doi:10.1175/JCLI-3243.1.

Stephens, G. L., and J. M. Haynes (2007), Near global observations of the warm rain coalescence process, *Geophys. Res. Lett.*, *34*, L20805, doi:10.1029/2007GL030259.

Stephens, G. L., et al. (2002), The CloudSat Mission and the A-Train, *Bull. Am. Meteorol. Soc.*, *83*(12), 1771–1790, doi:10.1175/BAMS-83-12-1771.

Stohl, A., K. Law, J. W. Bottenheim, P. Monks, and P. Quinn (eds.) (2010), POLARCAT (Polar Study Using Aircraft, Remote Sensing, Surface Measurements and Models of Climate, Chemistry, Aerosols, and Transport), *ACP Special Issue.*

Sun, Z., and K. P. Shine (1995), Parametrization of ice cloud radiative properties and its application to the potential climatic importance of mixed-phase clouds, *J. Clim*, *8*, 1874–1888, doi:10.1175/1520-0442(1995)008<1874:POICRP>2.0.CO;2.

Tanelli, S., S. L. Durden, E. Im, K. S. Pak, D. G. Reinke, P. Partain, J. M. Haynes, and R. T. Marchand (2008), CloudSat's cloud profiling radar after 2 years in orbit: Performance, external calibration, and processing., *IEEE Trans. Geosci. Remote Sens.*, *46*, 3560–3573, doi:10.1109/TGRS.2008.2002030.

Winker, D., W. Hunt, and M. J. McGill (2007), Initial performance assessment of CALIOP, *Geophys. Res. Lett.*, *34*, L19803, doi:10.1029/2007GL030135.

Winker, D. M., J. Pelon, and M. P. McCormick (2003), The CALIPSO mission: Spaceborne lidar for observation of aerosols and clouds, *Proc. SPIE Int. Soc. Opt. Eng.*, *4893*, 1–11, doi:10.1117/12.466539.

Winker, D. M., et al. (2010), The CALIPSO mission: A global 3D view of aerosols and clouds, *Bull. Am. Meteorol. Soc.*, *91*, 1211–1229, doi:10.1175/2010BAMS3009.1.

Yoshida, R., H. Okamoto, Y. Hagihira, and H. Ishimoto (2010), Global analysis of cloud phase and ice crystal orientation from cloud-aerosol lidar and infrared pathfinder satellite observation (CALIOP) data using attenuated backscattering and depolarization ratio, *J. Geophys. Res.*, *115*, D00H32, doi:10.1029/2009JD012334.

Zhang, D., Z. Wang, and D. Liu (2010), A global view of midlevel liquid-layer topped stratiform cloud distribution and phase partition from CALIPSO and CloudSat measurements, *J. Geophys. Res.*, *115*, D00H13, doi:10.1029/2009JD012143.

Zhou, C., P. Yang, A. E. Dessler, Y. Hu, and B. A. Baum (2012), Study of horizontally oriented ice crystals with CALIPSO observations and comparison with Monte Carlo radiative transfer simulations, *J. Appl. Meteorol. Climatol.*, *51*, 1426–1439, doi:10.1175/JAMC-D-11-0265.1.